2019

Combined Hardening Behavior for Sheet Metal and its Application

Nguyen Duc Toan

AIJR Publisher

More information about AIJR Books at –
https://books.aijr.org

Combined Hardening Behavior for Sheet Metal and its Application

by

Nguyen Duc Toan
Associate Professor,
School of Mechanical Engineering,
Hanoi University of Science and Technology, Vietnam

Published by
AIJR Publisher, 73, Dhaurahra, Balrampur, India 271604

Combined Hardening Behavior for Sheet Metal and its Application

Author
Nguyen Duc Toan
Associate Professor, School of Mechanical Engineering,
Hanoi University of Science and Technology,
1A-Dai Co Viet Street, Hai Ba Trung District, Hanoi City, Vietnam, 100000

About this Monograph

This book proposed modification hardening model to account for the expansion (isotropic) and translation (kinematic) of the yield loci in terms of the hardening model. The capability of the model is demonstrated by showing two characteristic effects of tension-compression and compression curves: crossing and Bauschinger effects.

ISBN: 978-81-936820-9-8 (eBook)
DOI: 10.21467/books.75

Type
Peer-reviewed

Published
14 August 2019

Number of Pages
84

Imprint
AIJR Books

Published by
AIJR Publisher, 73, Dhaurahra, Balrampur, India 271604

Table of Contents

List of Figures

List of Tables

Preface

Modeling the material behavior accurately in tension-compression and compression-tension load is essential to sheet metal forming simulation, failure and springback prediction, especially when the material points experience cyclic loadings. The combined linear hardening model proposed previously is modified to model the transient behavior more realistically by describing the scalar parameter β as a function of equivalent strain when compressive and reversed stress occurred.

This book proposed modification hardening model to account for the expansion (isotropic) and translation (kinematic) of the yield loci in terms of the hardening model. The capability of the model is demonstrated by showing two characteristic effects of tension-compression and compression curves: crossing and Bauschinger effects. Only modification of the scalar parameter β is added to describe the evolution of cyclic curves, which can be identified from tensile-compression tests and curve fittings. The proposed model is applied to sheet metal forming, fracture and springback predictions at room and elevated temperature. Tension-compression tests are firstly simulated and compared with available experimental data in order to fit and make the functions of scalar parameter β. The corrected data are then applied for complicated forming process e. g predict the fracture and improve the press formability of door hinge, the incremental sheet metal forming for complicate shape, and rotational incremental sheet forming for magnesium alloy sheets.

In order to predict the ductile fracture, a modification of combined kinematic and isotropic hardening law is implemented and evaluated from the histories of ductile fracture value (I) by means of finite element analysis. Here, the criterion for a ductile fracture, as developed by OYANE, (*Journal of Mechanical Work. Technol*ogy, 4 (1980), pp. 65–81), is carried out via a user material, using finite element code. To improve press formability and secure a safe product without any failure, the finite element method (FEM) simulations are coupled with Taguchi's orthogonal array experiment.

To improve press formability of a door hinge, three design variables – the die corner radius, declination of the bead punch, and peak angle of the bead punch – are selected to be improved. The numeric simulations reveal that the die corner radius is the most important variable, and its modification is most effective in improving the press formability for a door hinge. The simulation results are confirmed with experimental ones.

To simulate incremental sheet forming process for the product of complex shape (e.g. human face), a combination of both computer-aided manufacturing (CAM) and finite-element modelling (FEM) simulation, is utilized. Here, the results, using ABAQUS/Explicit finite-

element code, are compared with forming limit curve at fracture in order to predict and improve the forming conditions by changing process variables of tool radius, tool down-step, and friction coefficient. First, the CAM simulation is used to create cutter location data. This data are then calculated, modified, and exported to the input file format required by ABAQUS through using MATLAB programming. The FEM results are implemented for negative incremental sheet forming and then investigated by experiment

To simulate the effect of the large amount of heat generation at elements in the contact area due to friction energy of the rotational tool-specimen interface on equivalent stress-strain evolution in incremental forming, Johnson-Cook model was applied and also compared with equivalent stress-strain curves obtained by tensile test at elevated temperatures. The (FE) simulation results of ductile fracture was then compared with the experimental results of 80 mm × 80 mm × 25 mm square shape with 45 °, 60 °, and 80 mm × 80 mm × 20 mm square shape with 70 ° wall angles. The trend of (FE) simulation results were quite good agreement with experiment results. Finally, the effect of process parameters e. g tool down-step and tool radius on the ductile fracture value and forming limit curve at fracture (FLCF) were investigated using (FE) simulation results.

Dr. Nguyen Duc Toan

Chapter 1: Introduction

1.1 Motivation

Sheet forming parts has become a successful and well-established process for metals, alloys, polymers, ceramics and composites. Sheet forming may be used as final products or are subjected to further processing such as trimming, laze cutting, punching, etc. In either case, high strength and good formability are important properties and determine the success of sheet forming process and possibly that of subsequent operations. Process and properties optimization have always been a major concern in industrial practice. It is usually attempted by detailed considerations of die and punch design, lubrication, and proper selection of processing. The goal is to control the deformation during forming process and ensure minimum variation of local zone, avoidance of cracking (failure), dimensional control, and elimination of defects.

The process of sheet forming is a complex non-linear problem. When a force is applied on a forming tool, a number of mechanisms become involved in the transformation of the material into a die and became a well-defined shape. Normally, the following processes are involved in a typical sheet forming process:

- elastic deformation
- plastic deformation
- elastic recovery

Under the action of these mechanisms, the sheet forming process attains a level of deformation, which usually decreases with higher strength of material. The properties of material, such as relative density and strength, are not only related to the nature of the product, but also depend on the mode and history of externally applied forces. More specifically, stress loading path affects particle deformation and development of contact areas, which in turn affects the formability and springback of final products.

Since the mid-seventies, modeling of hardening behavior has provided an effective way to understand the basic mechanisms and optimize sheet forming process. These models are typically continuum mechanics-based phenomenological models. Currently, the use of these models in the finite element analysis has been successful in predicting failure and springback in complex shaped sheet forming.

In sheet metal forming applications, the non-monotonous deformation is especially important because reverse loading is commonly observed when sheet element moves through the tool

ISBN: 978-81-936820-9-8

AIJR Books
Thesis DOI: 10.21467/books.75

radii and draw beads. Also, when sheet parts are removed from tools after forming, material elements experience elastic unloading and spring-back. To describe the reverse loading behavior in the continuum phenomenological plasticity, there are two main approach, the first one based on kinematic hardening involving shifting of a single-yield surface and the second one involving multiple yield surfaces [1]. The simplest one in the former group is based on linear kinematic hardening proposed by Prager [2], Ziegler [3]. To add the transient behavior, the linear model was modified to nonlinear forms by Amstrong and Frederick [4] and Chaboche [5] by introducing an additional term to Prager's linear kinematic hardening model. Nonlinear and smooth deformation during loading and reverse loading were reproduced by introducing additional back stress term which makes total back stress decrease gradually with deformation. Several nonlinear kinematic hardening models based on Amstrong–Fredrick model have been emerged by introducing multiple back-stress terms [6] and [7] and translating limiting surface [8] and [9]. Two-surface models independently proposed by Krieg [10] and Dafalias and Popov [11] define the continuous variation of hardening between two yield surfaces. In the original multi-surface model proposed by Mroz [12], the predicted stress–strain curve is piecewise linear because of the constant plastic module [13]. Several multi/two-surface models have been proposed later[14], [15], [16], [17], [18], and [19] to analyze the one-dimensional cyclic behavior of solid structures at small strains. As a result, the prediction of fracture and spring-back with current models is not easy. The formation of parameters during loading and unloading, as well as the material elastic recovery may be confusing and also have a large effect on the final curve of prediction. With these in mind, the goal of this book is to make inroads on the understanding of the hardening behavior and propose a modification of hardening behavior to predict correctly the tension-compression curve in simple way. In the next section, we review the pertinent literature.

1.2 Literature review

In the past two decades, modeling and simulation play an increasingly important role in the design and optimization of sheet forming operations. The most common models are phenomenological and isotropic.

Various phenomenological hardening models, isotropic, kinematic and multi-surface, have been developed to reproduce hardening behavior of metals under various loading paths [2, 3, 12, 13, 20-24]. The simplest one, isotropic hardening model, uniformly extends a yield surface with fixed origin in stress space. The uniform extension implies that plastic deformation does not introduce further anisotropy and reduces any initial anisotropy. The isotropic hardening model can be adequate for FCC metals under monotonic loading, but it is not appropriate for materials under complex loading paths, where Bauschinger Effect or strength differential upon reverse loading is non-negligible. The isotropic hardening will introduce significant errors in the stress distribution of magnesium alloys undergone through sheet forming.

In contrast to the isotropic hardening model, a yield surface can translate in stress space with constant shape and size by a kinematic hardening model [13]. Various kinematic hardening models have been proposed to address Bauschinger Effect and cyclic plasticity [2, 4, 5]. One thermodynamical criterion for cyclic plasticity was summarized by Chaboche [5]: 'the current state of materials depends only on the current values of observable variables (total strain, temperature, etc.) and a set of internal-state variables'.

The classical kinematic hardening model of Prager can describe some Bauschinger Effect, but without transient yield upon reverse loading [2, 24, 25]. Back stress rate was assumed to be proportional to the plastic strain rate in Prager's model. This implies that continuous deformation encounters higher resistance than reverse loading. The main shortcoming of this model is that the stress strain relation is 'univocal' as a result of the assumed proportionality [5]. Another shortcoming is the inconsistency between different sub stress spaces. Ziegler model solved the problem of inconsistency, by translating the yield surface in radial directions [3].

Linearity in stress strain behavior and sharp reverse yield induced by Prager's model were avoided by two- or multi-surface models [10, 11, 12, 20]. Only one yield surface was active at a given instant in time in the two- or multi-surface models. A large number of yield surfaces are needed to describe material behaviors in the multi-surface models, because of their piecewise linearity in stress strain behaviors. The two-surface model can predict cyclic plasticity well by introducing continuous variation of hardening modulus to translate the active yield surface, although it has its disadvantages discussed by Chaboche [5].

Based on Prager's model, Armstrong and Frederick [4] proposed a nonlinear kinematic hardening model by introducing a recall term for back stress evolution. Chaboche [5] further developed it, by including multiple back stresses to more accurately model cyclic plasticity. Nonlinearity and smooth transient behavior upon reverse loading were reproduced by the recall term. The recall term implies that the effect of earlier plastic deformation on back stress decreases gradually with progressive deformation. This reflects the fact that microstructure from the recent deformation history contributes greater to the back-stress evolution than does the deformation occurring earlier.

More complex anisotropic hardening models have been proposed during last decade to consider microstructure evolution in steels subjected to arbitrary loading path change at moderate to large deformation [26-31]. Three internal state variables, (**S**, **P**, **X**), were introduced to describe 'directional strength of planar persistent dislocation structures' **S**, its polarity **P**, and back stress **X** induced by dislocation pile-ups. The evolution of these state variables was specified on the basis of experimental observations of the evolution of dislocation structure, such as depolarization and disintegration of preformed dislocation structure under reverse loading. The effect of prestrain on hardening in subsequent deformation can be predicted by this model. However, texture evolution is not considered

explicitly, although initial plastic anisotropy induced by texture was incorporated in the model by a fourth-order tensor. The accuracy of model prediction at large strains would be improved by considering texture evolution.

1.3 Goals of this book

We believe that better understanding the role of hardening behavior is the key to better predict the tension-compression and compression-tension curves. The major goal of this dissertation is to give the simple way to determine correctly stress-strain curves with revered load, and then predict fracture obeyed ductile fracture criterion, therefore to provide a design tool to control and optimize the sheet forming operations. The specific goals of this study are outline below:

- In chapter 2 we identify the capabilities and limitations of phenomenological models on predicting such as the stress and strain curve evolution as well as the fracture tendency. To do this, we implemented one of the most popular phenomenological models – combined kinematic/isotropic model into finite element program (ABAQUS/EXPLICIT) and developed a robust user subroutine, which provides a useful tool to study formability of sheet forming process. After that we propose a modification of hardening law to predict correctly stress-strain curves with reverted load.
- In chapter 3, using the developed VUMAT, we analyzed, predicted fracture and optimized press formability of a door hinge.
- Incremental sheet forming for complex shape are modeled and studied with respect to the effect of parameters on incremental forming method and its improvements in chapter 4. A combination of both CAM and FEM simulation is implemented and evaluated from the histories of stress and strain value by means of finite element analysis. Then, the results, using ABAQUS/Explicit finite element code, are compared with forming limit curve at fracture (FLCF) and also ductile fracture criterion via VUMAT subroutine in order to predict and improve the forming conditions by changing process variables of tool radius, tool down-step and friction coefficient according to the orthogonal array of Taguchi's method.
- Chapter 5 contains a study of rotational incremental forming for magnesium alloy sheet. As the ductile failure criterion, the Oyane's fracture criterion via VUMAT user material based on a combined kinematic/isotropic hardening law and Johnson-Cook model is used to predict fracture at elevated temperatures which was generated by rotational tool and friction energy at the tool-specimen interface. The simulation results were used to predict forming limit curve for rotational incremental forming and study the effect of process parameters on ductile fracture value.

Chapter 2: Continuum Mechanics Models and Development of VUMAT

2.1 Introduction

The finite element analysis of many sheet forming problems faces often difficulties due to the strongly non-linear material behavior including friction which makes convergence difficult in implicit finite element schemes. Such problems can be better addressed within the framework of explicit schemes (such as ABAQUS/Explicit) especially when coupled with a remeshing strategy. The library of ABAQUS contains several constitutive models including isotropic hardening model kinematic hardening model and combined hardening model. Unfortunately, the version available in ABAQUS is not versatile enough as a number of parameters are considered to be constant. This problem is addressed in ABAQUS/Standard with the used of field variables and user subroutine "USDFLD" which is not available in EXPLICIT.

For this reason, we developed a VUMAT user subroutine for the most general version of combined isotropic/ kinematic hardening model for ABAQUS/EXPLICIT. In this chapter, we firstly present a summary of the combined hardening model and its calibration, as well as an integration model for the model and then we propose the modification of combined hardening model to predict correctly the stress-strain curves with reverted load and its validation.

2.2 Constitutive Models

In this study, the program is written in modular form so that different material models can be added in the future. At the present time there are seven continuum material models, although the isothermal elastic/plastic model is the only continuum model described here.

The main assumption is that the strain rate is constant from time t_{n_1} to t_n. During each conjugate gradient iteration, the latest values of the kinematic quantities are used to update the stress. All material models are written in terms of the un-rotated Cauchy stress σ and the deformation rate d in the un-rotated configuration. When calculating linear elastic material response, Hooke's law is used. In a rate form, this is written as

$$\dot{\sigma} = \lambda trace(d)\delta + 2\mu d \qquad (2.1)$$

where λ and μ are the elastic Lame material constants.

ISBN: 978-81-936820-9-8
Thesis DOI: 10.21467/books.75

2.2.1 Basic Definitions and Assumptions

Some definitions and assumptions are outlined here. In Figure 2.1, which geometrically depicts the yield surface in deviatoric stress space, the back stress (the center of the yield surface) is defined by the tensor α. If σ is the current value of the stress, the deviatoric part of the current stress is

$$S = \sigma - \frac{1}{3} trace(\sigma)\delta \tag{2.2}$$

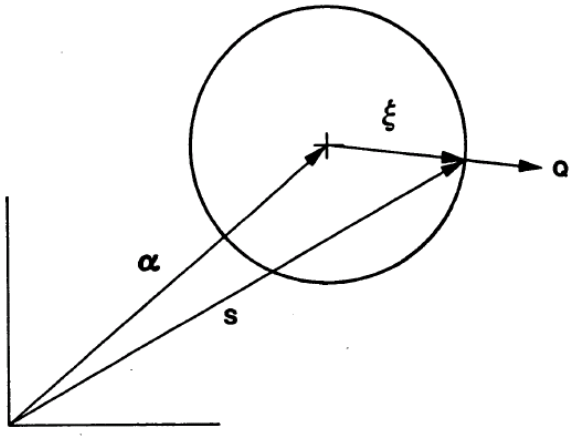

Figure 2.1: *Yield surface in deviatoric stress space.*

The stress difference is then measured by subtracting the backstress from the deviatoric stress by

$$\xi = S - \alpha \tag{2.3}$$

The magnitude of the deviatoric stress difference R is defined by

$$R = \|\xi\| = \sqrt{\xi : \xi} \tag{2.4}$$

where the inner product of second order tensors is $S : S = S_{ij}S_{ij}$. Note that if the back stress is zero (isotropic hardening case) the stress difference is equal to the deviatoric part of the current stress S.

The von Mises yield surface is defined as

$$f(\sigma) = \frac{1}{2}\xi : \xi = \kappa^2 \tag{2.5}$$

and the von Mises effective stress is defined by

$$\bar{\sigma} = \sqrt{\frac{3}{2}\xi : \xi} \tag{2.6}$$

Since R is the magnitude of the deviatoric stress tensor when $\alpha = 0$, it follows that

$$R = \sqrt{2}\kappa = \sqrt{\frac{2}{3}}\bar{\sigma} \tag{2.7}$$

The normal to the yield surface can be determined from Equation 2.5:

$$\boldsymbol{Q} = \frac{\boldsymbol{\partial f/\partial \sigma}}{\|\boldsymbol{\partial f/\partial \sigma}\|} = \frac{\boldsymbol{\xi}}{\boldsymbol{R}} \tag{2.8}$$

It is assumed that the strain rate can be decomposed into elastic and plastic parts by an additive decomposition,

$$d = d^{el} + d^{pl} \tag{2.9}$$

and that the plastic part of the strain rate is given by a normality condition,

$$d^{pl} = \gamma Q \tag{2.10}$$

where the scalar multiplier γ is to be determined.

A scalar measure of equivalent plastic strain rate is defined by

$$\bar{d}^{pl} = \sqrt{\frac{2}{3} d^{pl} : d^{pl}} \tag{2.11}$$

which is chosen such that

$$\bar{\sigma}\bar{d}^{pl} = \sigma : \Delta\, \varepsilon^{pl} \tag{2.12}$$

The stress is expressed in rate is assumed to be purely due to the elastic part of the strain rate and terms of Hooke's law by

$$\dot{\sigma} = \lambda trace(d^{el})\delta + 2\mu d^{el} \tag{2.13}$$

where λ and μ are the Lame constants for the material.

In what follows, the theory of isotropic hardening, kinematic hardening, and combined hardening is described.

2.2.2 Isotropic Hardening

In the isotropic hardening case, the back-stress is zero and the stress difference is equal to the deviatoric stress S. The consistency condition is written by taking the rate of Equation 2.5:

$$\dot{f}(\sigma) = 2\kappa\dot{\kappa} \tag{2.14}$$

The consistency condition requires that the state of stress must remain on the yield surface at all times. The chain rule and the definition of the normal to the yield surface given by Equation 2.8 is used to obtain

$$\dot{f}(\sigma) = \frac{\partial f}{\partial \sigma} : \dot{\sigma} = \left\| \frac{\partial f}{\partial \sigma} \right\| Q : \dot{\sigma} \tag{2.15}$$

and from Equations 2.4 and 2.5,

$$\left\| \frac{\partial f}{\partial \sigma} \right\| = \|S\| = R \tag{2.16}$$

Combining Equations 2.14, 2.15, and 2.16,

$$\frac{1}{R} S : \dot{\sigma} = \dot{R} \tag{2.17}$$

Note that because S is deviatoric, $S : \dot{\sigma} = S : \dot{S}$, and

$$S : \dot{S} = \frac{d}{dt}\left(\frac{1}{2} S : S\right) = \frac{d}{dt}\left(\frac{\bar{\sigma}^2}{3}\right) = \frac{2}{3}\bar{\sigma}\dot{\sigma} \tag{2.18}$$

Then Equation 2.17 can be written as

$$\dot{R} = \sqrt{\frac{2}{3}}\dot{\bar{\sigma}} = \sqrt{\frac{2}{3}} H' \dot{\bar{d}}^{pl} \tag{2.19}$$

where *H'* is the slope of the effective stress versus equivalent plastic strain ($\bar{\sigma}$ vs. $\bar{\varepsilon}^{pl}$). This may be derived from uniaxial tension test data as shown in Figure 2.2.

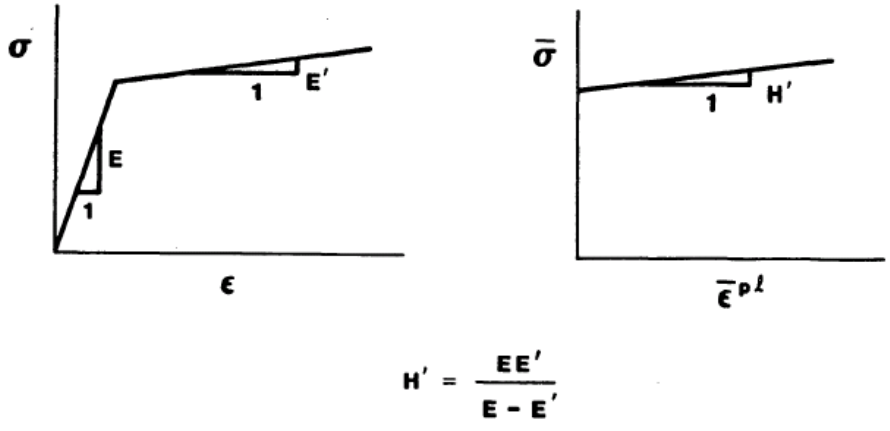

Figure 2.2: *Conversion of data from a uniaxial tension test to equivalent plastic strain versus von Mises stress.*

The consistency condition (Equation 2.17) and Equation 2.19 result in

$$\sqrt{\frac{2}{3}} H' \dot{\bar{d}}^{pl} = Q : \dot{\sigma} \tag{2.20}$$

The trial elastic stress rate $\dot{\sigma}^{tr}$ is defined by

$$\dot{\sigma}^{tr} = C : d \tag{2.21}$$

where C is the fourth-order tensor of elastic coefficients defined by Equation 2.13. Combining the strain rate decomposition defined in Equation 2.9 with Equations 2.20 and 2.21 yields

$$\sqrt{\frac{2}{3}} H' \dot{\bar{d}}^{pl} = Q : \dot{\sigma}^{tr} - Q : C : d^{pl} \tag{2.22}$$

Since Q is deviatoric, $C: Q = 2\mu Q$ *and* $Q: C: Q = 2\mu$. Then using the normality condition (Equation 2.10), the definition of equivalent plastic strain (Equation 2.11), and Equation 2.22,

$$\frac{2}{3} H' \gamma = Q : \dot{\sigma}^{tr} - 2\mu\gamma \tag{2.23}$$

and since Q is deviatoric ($Q : \dot{\sigma}^{tr} = 2\mu Q : d$), γ is determined from Equation 2.23 as

$$\gamma = \frac{1}{\left(1+\frac{H'}{3\mu}\right)} Q : d \tag{2.24}$$

The current normal to the yield surface Q and the total strain rate d are known quantities. Hence, from Equation 2.24, γ can be determined and then used in Equation 2.10 to calculate the plastic part of the strain rate. With the additive strain rate decomposition and the elastic stress rate of Equations 2.9 and 2.13, this completes the definition of the rate Equations.
The means of integrating the rate Equations, subject to the constraint that the stress must remain on the yield surface, still remains to be explained. How that is accomplished will be shown in Section 2.3.2.

2.2.3 Kinematic Hardening

For kinematic hardening, the von Mises yield condition is written in terms of the stress differenceξ:

$$f(\xi) = \frac{1}{2} \xi : \xi = \kappa^2 \tag{2.25}$$

It is important to remember that both ξ and the back stress α are deviatoric tensors.
The consistency condition for kinematic hardening is written as

$$\dot{f}(\xi) = 0 \tag{2.26}$$

because the size of the yield surface does not grow with kinematic hardening ($\dot{\kappa} = 0$). Using the chain rule on Equation 2.26, and

$$\frac{\partial f}{\partial \xi} : \dot{\xi} = 0 \tag{2.27}$$

$$\frac{\partial f}{\partial \xi} = \left\| \frac{\partial f}{\partial \xi} \right\| Q = RQ \tag{2.28}$$

Combining Equations 2.27 and 2.28 and assuming that *R # 0,*

$$Q : \dot{\xi} = 0 \tag{2.29}$$

or

$$Q : (\dot{S} - \dot{\alpha}) = 0 \tag{2.30}$$

A geometric interpretation of Equation 2.30 is shown in Figure 2.3 in which the back-stress moves in a direction parallel to the normal to the yield surface.

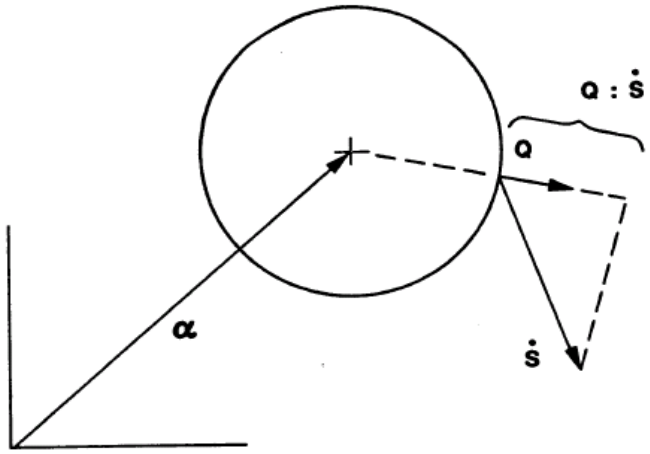

Figure 2.3: *Geometric interpretation of the consistency condition for kinematic hardening.*

The back-stress rate $\dot{\alpha}$ must now be defined. For the isotropic hardening case (Equation 2.20),

$$Q : \dot{\sigma} = \sqrt{\frac{2}{3}} H' \bar{d}^{pl} = \frac{2}{3} H' \gamma \tag{2.31}$$

The kinematic hardening condition assumes that

$$\dot{\alpha} = \Phi d^{pl} = \Phi \gamma Q \tag{2.32}$$

where Φ is a material parameter. If Φ is chosen to be *(2/3) H',* Equations 2.32 and 2.30 give a result identical to the isotropic hardening case (Equation 2.31). Hence, either Equation 2.31 or 2.32 gives us a scalar condition on$\dot{\alpha}$. Both of these are assumptions and must be shown to be reasonable. Experience with material models based on these assumptions has shown that, in fact, they are reasonable representations of material behavior.

Using Equation 2.32, Equation 2.9 (the strain rate decomposition), and Equation 2.13 (the elastic stress rate) in Equation 2.30 (the consistency condition for kinematic hardening) gives

$$Q:(\dot{\sigma}^{tr} - C:d^{pl}\quad) = Q:\frac{2}{3}H'\gamma Q \tag{2.33}$$

Using the normality condition ($d^{pl} = \gamma Q$) and the fact that Q is deviatoric, $C:Q = 2\mu Q$. Solving Equation 2.33 for γ then gives

$$\gamma = \frac{1}{\left(1+\frac{H'}{3\mu}\right)}Q:d \tag{2.34}$$

which is the same result as that of the isotropic hardening case.

2.2.4 Combined Isotropic and Kinematic Hardening

For the combined hardening case, a scalar parameter β is defined as ranging from 0 to 1, which determines the relative amount of each type of hardening. Figure 2.4 illustrates the uniaxial response to reversed loading that results from different choices of β. When β = 0, only kinematic hardening occurs, and when β = 1, only isotropic hardening occurs.

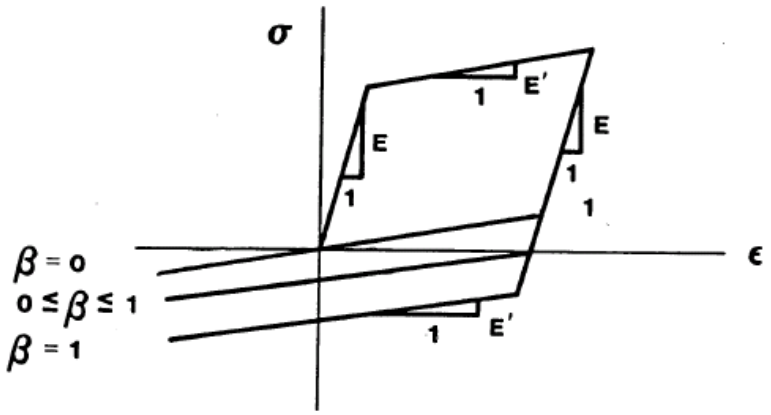

Figure 2.4: *Effect of the hardening parameter β on uni-axial response.*

The results derived for the independent hardening cases are multiplied by the appropriate fraction for each type of hardening. Equations 2.19 and 2.32 are rewritten as

$$R = \sqrt{\frac{2}{3}}H'\bar{d}^{pl}\beta \tag{2.35}$$

$$\dot{\alpha} = \frac{2}{3}H'd^{pl}(1-\beta) = \frac{2}{3}H'\gamma Q(1-\beta) \tag{2.36}$$

As before, the consistency condition is

$$Q:\dot{\xi} = \dot{R} \tag{2.37}$$

or

$$Q:(\dot{S} - \dot{\alpha}) = \sqrt{\frac{2}{3}}H'\bar{d}^{pl}\beta \tag{2.38}$$

Using the elastic stress rate, the additive strain rate decomposition, and the normality condition, $Q:\dot{S} = Q:(\dot{\sigma}^{tr} - \gamma C:Q)$ Together with Equations 2.36 and 2.11, this transforms Equation 2.38 into

$$Q:\dot{\sigma}^{tr} - \gamma Q:C:Q - \frac{2}{3}H'\gamma Q(1-\beta)Q:Q = \sqrt{\frac{2}{3}}H'\beta\sqrt{\frac{2}{3}(\gamma Q):(\gamma Q)} \quad (2.39)$$

Solving for γ,

$$\gamma = \frac{1}{\left(1+\frac{H'}{3\mu}\right)}Q:d \quad (2.40)$$

which is the same result as was obtained for each of the independent cases.

The following is a summary of the governing Equations for the combined theory:

$$\dot{\sigma} = C:(d - d^{pl}) = \dot{\sigma}^{tr} - 2\mu\gamma Q \quad (2.41)$$

$$\dot{R} = \beta\sqrt{\frac{2}{3}}H'\bar{d}^{pl} = \beta\frac{2}{3}H'\gamma \quad (2.42)$$

$$\dot{\alpha} = (1-\beta)\frac{2}{3}H'd^{pl} \quad (2.43)$$

$$d^{pl} = \begin{cases} 0(elastic), & if \quad f(\xi) < \kappa^2 \\ \gamma Q(plastic), & if \quad f(\xi) \geq \kappa^2 \end{cases} \quad (2.44)$$

$$\gamma = \frac{1}{\left(1+\frac{H'}{3\mu}\right)}Q:d \quad (2.45)$$

$$Q = \frac{\partial f/\partial\sigma}{\|\partial f/\partial\sigma\|} = \frac{\xi}{R} \quad (2.46)$$

2.3 Implementation of Combined Hardening Law and Development of VUMAT

The constitutive model presented in the previous section was implemented in the ABAQUS, a general-purpose finite element program [32]. This code provides a general interface for user programmed constitutive models through a "user subroutine" (VUMAT for ABAQUS/Explicit). As discussed above, we develop our own user subroutine because the versions of hardening behavior models in ABAQUS/Explicit are not flexible enough. Figure 2.5 shows schematically the integration procedure in ABAQUS/Explicit with a VUMAT. For each time step, ABAQUS integrates the Equations of equilibriums based on the stress state at the beginning of the step at each integration point and provides the deformation gradient for VUMAT subroutine. VUMAT then finishes the integration of the constitutive model and updates the stress and state variable for each integration point. With the information that VUMAT provides, ABAQUS can then continue the calculation for the next time step.

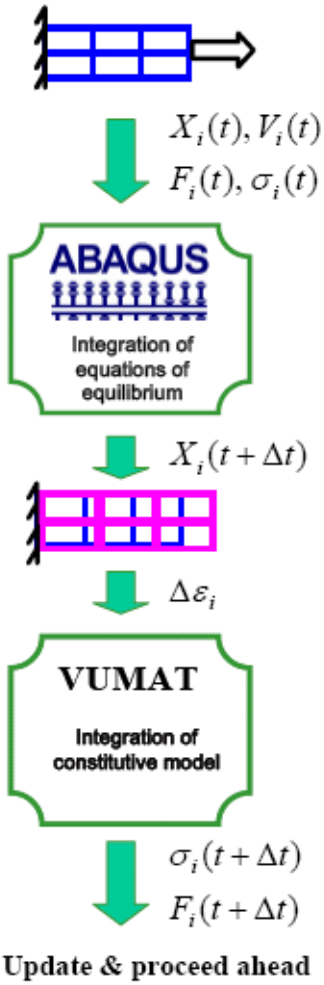

Figure 2.5: *ABAQUS and VUMAT subroutine.*

2.3.1 Derivation of the Constitutive Equations Elasticity

A basic assumption of elastic-plastic models is that the deformation can be divided into an elastic part and an inelastic (plastic) part. There are mainly two methods of decomposition of kinematics: (a) multiplicative decomposition $\mathbf{F} = \mathbf{F}^{el}\mathbf{F}^{pl}$, in which it requires that the plastic deformation gradient $\mathbf{F}^{pl}$ (9 elements) is stored as a state variable for all integration points. (b) additive decomposition: $\Delta\varepsilon = \Delta\varepsilon^{el} + \Delta\varepsilon^{pl}$ where $\Delta\varepsilon$ is the total strain increment, $\Delta\varepsilon^{el}$ is the increment of the elastic strain, and $\Delta\varepsilon^{pl}$ is the increment of inelastic strain. The additive decomposition is adequate when the elastic strains are small. For a linear and isotropic material:

$$\Delta\sigma = C\Delta\varepsilon^{el} = C(\Delta\varepsilon - \Delta\varepsilon^{pl}) \text{ with } C \equiv 2GI + (K - 2G/3)\delta:\delta \qquad (2.47)$$

where $\mathbf{C}$ is the forth order elasticity tensor, $\boldsymbol{I}$ and $\boldsymbol{\delta}$ are respectively the forth and second order identity tensor, G and K are the shear modulus and bulk modulus respectively which are

functions of powder porosity. For isotropic materials, $G = \frac{E}{2(1+\nu)}$ and$K = \frac{E}{3(1-2\nu)}$ where E and ν are Young's modulus and Poisson's ratio, respectively.

Plasticity: The evolution Equation for the plastic part of the deformation gradient ("flow rule") is given by $\Delta\bar{\varepsilon}^{pl} = \Delta\gamma Q$ where, $\Delta\gamma$ will be determined in Section 2.3.2. The details of time integration procedure are discussed below.

2.3.2 Integration procedure

For a typical time step, our VUMAT uses explicit Euler algorithm (Euler forward) to integrate stresses and internal state variable. The time increment is limited by the overall stability limit of the explicit integration of the Equations of motion. This is usually more restrictive than the stability limit of the stress integration in the VUMAT. Other integration algorithms are also can be used, such as implicit Euler algorithm (Euler backward) [33, 34] or semi-implicit Euler algorithm [35]. Since the stability constrain limits the overall time increment, explicit and semi-explicit methods (i.e. not iterative methods) are more efficient than fully implicit which are more appropriate for large time steps and plastic strain increments. The VUMAT uses the stress and internal variables at the beginning of an increment and the strain increment provided by ABAQUS and needs to predict the stress at the end of the increment, as well as the new values of the internal state variables.

The increment of strain across a time step $\Delta t = t_{n+1} - t_n$ is

$$\Delta\varepsilon_{n+1} = \Delta\varepsilon^{el}_{n+1} + \Delta\varepsilon^{pl}_{n+1} \tag{2.48}$$

The finite element algorithm requires an incremental form of Equations 2.41 through 2.46. Additionally, an algorithm must be used that integrates the incremental Equations subject to the constraint that the stress remains on the yield surface.

The incremental analogs of Equations 2.41 through 2.43 are

$$\sigma_{n+1} = \sigma^{tr}_{n+1} - 2\mu\Delta\gamma Q \tag{2.49}$$

$$R_{n+1} = R_n + \frac{2}{3}\beta H'\Delta\gamma \tag{2.50}$$

$$\alpha_{n+1} = \alpha_n + (1-\beta)\frac{2}{3}\Delta\gamma H'Q \tag{2.51}$$

where $\Delta\gamma$ represents the product of the time increment and the equivalent plastic strain rate ($\Delta\gamma = \dot{\gamma}\Delta t$) The subscripts n and n + 1 refer to the beginning and end of a time step, respectively; H, the slope of the uniaxial yield stress versus the plastic strain curve, is calculated by Equations (2.52), and β, the scalar parameter, is defined as ranging from 0 to 1. When β =

0, only kinematic hardening occurs, and when β=1, only isotropic hardening occurs. For isotropic/kinematic hardening, β is determined by comparing cyclic tensile curves between experiment data and simulation data.

$$H = \frac{d\bar{\sigma}}{d\bar{\varepsilon}} = Kn\left(\varepsilon_0 + \bar{\varepsilon}_{pl}\right)^{n-1} \tag{2.52}$$

For nonlinear isotropic/kinematic hardening model, the size of yield surface was modified as a function of equivalent plastic strain $\bar{\varepsilon}_P$ and has the relationship with Swift's work-hardening law Equation (2.53) following Equation (2.54)

$$\bar{\sigma}(\bar{\varepsilon}_{pl}) = K(\varepsilon_0 + \bar{\varepsilon}_{pl})^n \rightleftarrows \tag{2.53}$$

$$\bar{\sigma}_Y(\bar{\varepsilon}_{pl}) = \bar{\sigma}(\bar{\varepsilon}_{pl}) - H\bar{\varepsilon}_{pl} \tag{2.54}$$

An incremental analog is needed for the rate forms of the consistency condition given by Equations 2.14, 2.26, and 2.38. At the end of the time step, the stress state must be on the yield surface. Hence, the incremental consistency condition is

$$\alpha_{n+1} + R_{n+1}Q = S_{n+1} \tag{2.55}$$

Equation 2.50 is depicted in Figure 2.6.

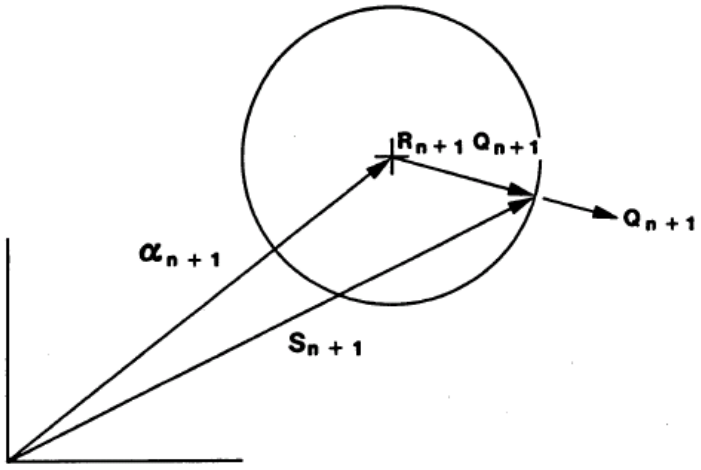

Figure 2.6: *Geometric interpretation of the incremental form of the consistency Condition for combined hardening.*

Substituting the definitions given by Equations 2.49 through 2.50 into the consistency condition of Equation 2.55,

$$\left[\alpha_n + (1-\beta)\frac{2}{3}H'\Delta\gamma Q\right] + \left[R_n + \frac{2}{3}\beta H'\Delta\gamma\right]Q = S_{n+1}^{tr} - 2\mu\Delta\gamma Q \tag{2.56}$$

Taking the tensor product of both sides of Equation 2.56 with Q and solving for $\Delta\gamma$,

$$\Delta\gamma = \frac{1}{2\mu}\frac{1}{\left(1+\frac{H'}{3\mu}\right)}\left(\|\xi_{n+1}^{tr}\| - R_n\right) \tag{2.57}$$

It follows from Equation 2.57 that the plastic strain increment is proportional to the magnitude of the excursion of the elastic trial stress past the yield surface (see Figure 2.6). Using the result of Equation 2.57 in Equations 2.49 through 2.51 completes the algorithm. In addition,

$$\Delta d^{pl} = \Delta\gamma Q \tag{2.58}$$

and

$$\Delta\bar{d}^{pl} = \sqrt{\frac{2}{3}}\Delta\gamma \tag{2.59}$$

Using Equation 2.57 in Equation 2.49 shows that the final stress is calculated by returning the elastic trial stress radially to the yield surface at the end of the time step (hence the name Radial Return Method). Estimates of the accuracy of this method and other methods for similarly integrating the rate Equations are available in Krieg and Krieg [28] and Schreyer et al. [29]. The radial return correction (the last term in Equation 2.49) is purely deviatoric. The summary of numerical integration algorithm of model is depicted in Figure 2.7.

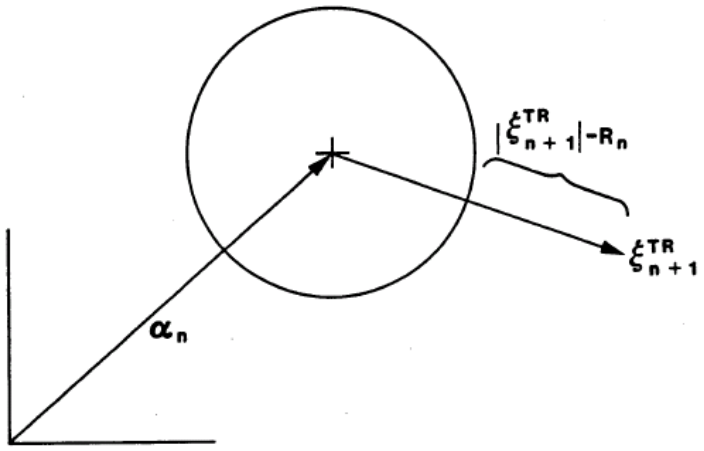

Figure 2.7: *Geometric interpretation of the radial returned correction.*

2.3.3 Verification of VUMAT subroutine

Above constitutive model is implemented into a commercial finite element program ABAQUS/Explicit via VUMAT user material for the uni-axial tension-compression and compression-tension tests with standard ASTM specimens for material of magnesium alloy

sheet which having rectangular cross-section of 13 mm width by 3.2 thickness and a gage length of 50 mm. in order to prevent buckling occurrence, a test method developed by Boger et al. [9], which relies on through-thickness sheet stabilization to avoid buckling, was used to extend the attainable strain range of Mg sheet in compression to approximately −0.08. A schematic of the novel tension/compression test [9] and the sample dimensions are shown in Figure 2.8 (a) two flat steel plates and a hydraulic cylinder system were used to provide side force to support the exaggerated dog-bone specimen. Side forces of 12 kN were used to stabilize the sheet sample. Figure 2.8 (b) shows the finite-element model of ABAQUS version 6.5 for test process. Here, the blank modeled using solid elements C3D8R, and the flat steel plate modeled using rigid surface-elements R3D4.

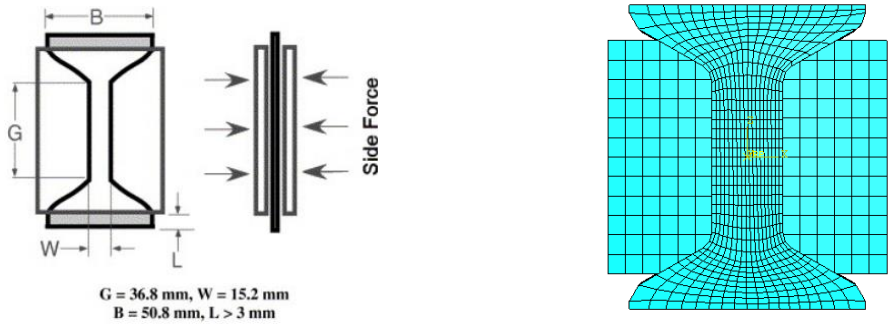

Figure 2.8: *Schematic of the novel tension/compression test [9]*

The average element size of the solid elements was about 1mm in width, 2mm in length, and 1mm in height. Meanwhile, the average element size of the rigid surface-elements was about 2 mm in width, and 2 mm in length. The friction coefficient μ at the blank/flat plate interface, μ_2=0.1, was assumed for all the simulations. The other material parameters are listed in Table 2.1.

Table 2.1: *Mechanical properties of tested material (Magnesium alloy sheet)*

Material	**AZ31B**
Density (r, kg/cm^3)	1.77e-06
Young's modulus (E, kN/cm^2)	45000
Possion's ratio	0.35
Tension yield stress (MPa) (σ_Y^T)	220
Compression yield stress (MPa) (σ_Y^C)	120
ε_0	0.005
K (MPa)	365.09
n	0.124

Figure 2.9 shows the comparisons between the FE simulation and experiment results. The best fit for uni-axial tensile test and Bauschinger effect was chosen with the scalar parameter β of 0.5. However, there are discrepancies between theoretical models and the test data in others zone. Therefore, in this chapter we have modified the hardening law to predict correctly behavior of stress-strain curves at reversed load for Mg alloy and also all others kind of materials.

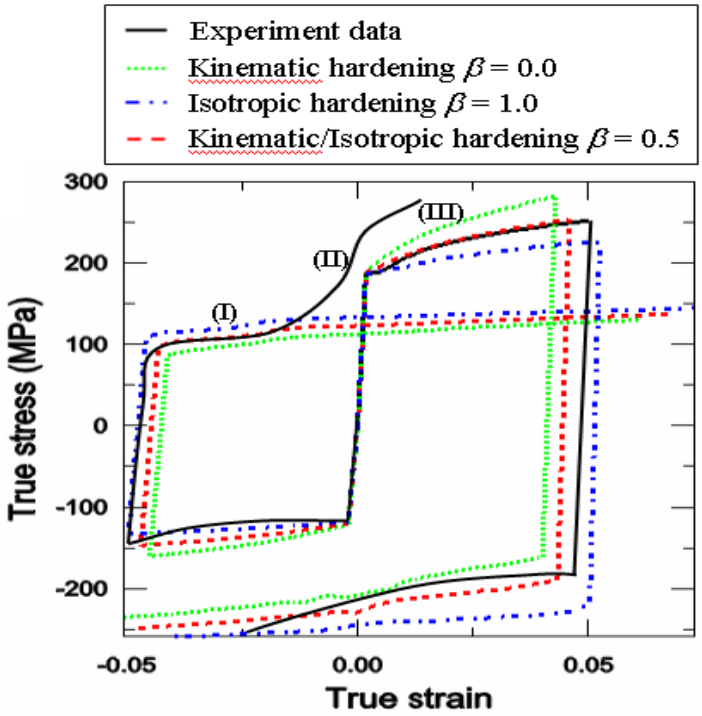

Figure 2.9: *The comparisons between the experiment result and FE simulation results of combined kinematic/isotropic hardening.*

2.3.4 A Modification of Combined Non-linear Hardening

As shown in Figure 2.9, when β changes from 0.0 to 1.0 the directions of cyclic tensile curves will be changed. It means that, if we can present β as a function of equivalent strain then we can predict correctly the shapes of stress-strain curves at compression and reversed stress. In this study, we proposed β as exponential function of equivalent strain. In compression stress, the scalar parameter β is expressed as below:

$$\beta^C = \beta_0 - F(\varepsilon^{pl(C)})^m \tag{2.60}$$

where β_0 is the initial direction of stress-strain curves when compression stress occurs. Here, $\beta_0 = 1$ is chosen to follow isotropic hardening direction. F and m are determined by fitting the generated curve from simulation with experiment data and chosen the best fit as F of 2.016e07 and m of 5 for Mg alloy sheet.

In case of reversed stress occurrence for compression-tension tests, as depict in Figure 2.9, the curve should be divided by three sections. The first section is formulated as Equation (2.61)

$$\beta_{R1}^{C-T} = \beta_0 - F_1(\varepsilon_R^{pl(C-T)})^{m1} \quad (2.61)$$

here, β_0 = 1, F_1 and m_1 was estimated as 1.952e08 and 5 for Mg alloy sheet, respectively. The second section is expressed as Equation (2.62) when $\varepsilon_R^{pl(C-T)}$ is greater than 0.04 mm.

$$\beta_{R2}^{C-T} = F_2(\varepsilon_R^{pl(C-T)})^{m2} \quad (2.62)$$

Similarly, F_2 and m_2 was estimated as 1.53e03 and 0.2 for Mg alloy sheet, respectively. The third section is generated when β_{R2}^{C-T} reaches β = 0.5 of fitting curve for uni-axial tensile test then $\beta_{R2}^{C-T} = 0.5$.

Figure 2.10 (a) shows the comparison of the measured continuous uni-axial tension-compression (T-C) and compression-tension (C–T) tests to the results calculated from the finite element simulations with proposed models. The results of proposed model are good agreement with measurements. Figure 2.10 (b) present the results of tension-compression (T-C) and compression-tension (C–T) FE simulation with various of pre-strain. To investigate this hardening model, finite element analysis of three-point bending-unbending test for the magnesium alloy sheet modeled using solid elements C3D8R is validated. The simulation results are depicted and plotted in Figure 2.11. In FE simulation result of three-point bending-unbending for solid elements, we can check tension-compression and compression-tension curves for correlative elements at the same time. The proposed hardening law simulates forward bending-unbending quite well comparing with tension-compression and compression-tension test in Figure 2.10

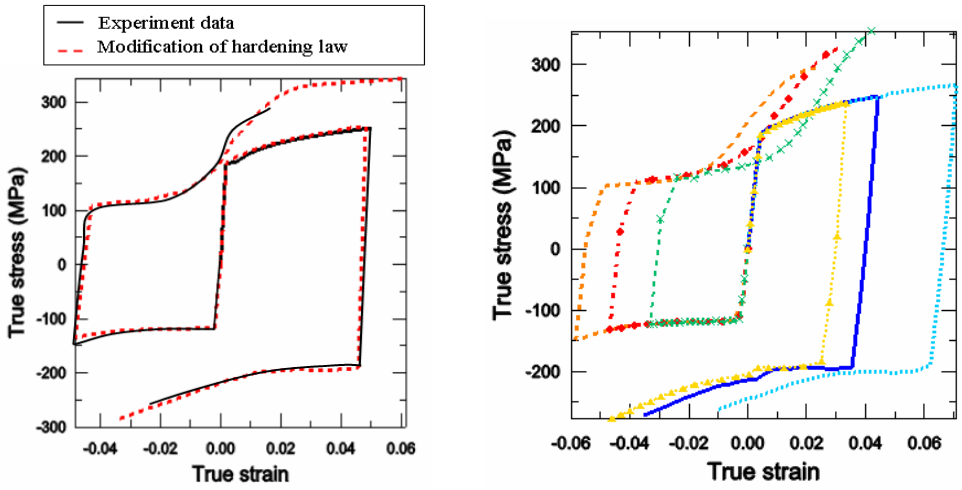

(a) (b)

Figure 2.10: *Uni-axial tension-compression (T-C) and compression-tension (C–T) simulation results of proposed model comparing with experiment data (a) and with various of pre-strain (b)*

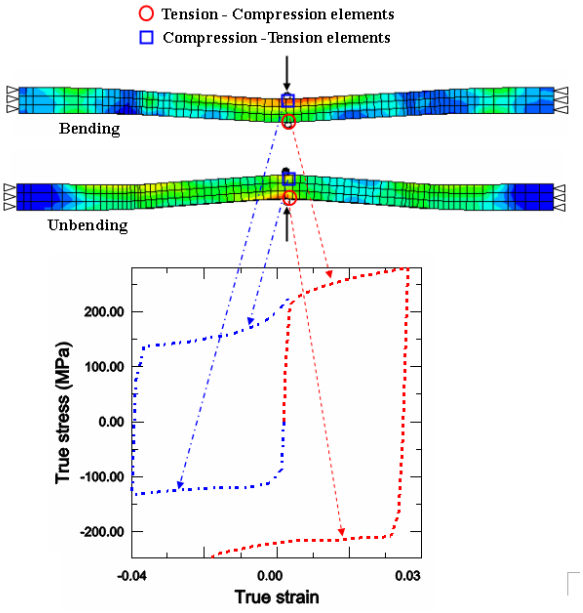

Figure 2.11: *FE simulation results for three-point bending-unbending process*

Chapter 3: Application of Proposed Hardening Model to Predict Fracture and Improve Press Formability of Door Hinge

3.1 Introduction

Door hinges are a key product in the automotive industry, and their functions include not only opening and closing the door or keeping the door open at a certain angle, but also reducing passenger trauma in the case of a collision. Car door hinges are produced by punching and then forming a plate to obtain the desired geometry. Door hinges can take many shapes, depending on the type of automobile, front or rear door, designer, and producer. In addition, there are many processing parameters that contribute to the formability of a door hinge, such as the material properties, forming conditions, geometric shapes of the die and punch, and geometric shapes of the blanks etc., which in turn determine the press formability, as regards the thickness variation, and blank failure after the forming. However, due to the increasing demand for light-weight, high-strength and corrosion-resistant materials, many new materials have been developed for application in automobiles. Yet, these materials, especially high-strength steel sheet, tend to have less formability than the conventional materials used for sheet forming, resulting in the frequent failure of door hinge products. When manufacturing a door hinge, as shown in Figure 3.1, product failure frequently occurs in the critical area when subjected to serious strain during the forming process and found to be prone to internal or superficial micro-defects due to excessive tensile stress [36]. This initial damage and its growth then cause quality problems, such as necking and fractures, due to ductile tearing of the sheet.

Figure 3.1: *Typical failure of a door hinge in critical area*

ISBN: 978-81-936820-9-8
Thesis DOI: 10.21467/books.75

To predict material fractures several researches had been proposed [37, 38]. Among the various methods, Clift et al. [39] concluded that the existing ductile fracture criteria were more accurate than other methods. To improve the formability of sheet material, Kim and Park [40] used FE simulations according to the orthogonal array of Taguchi's method [41-43] to determine the effect of forming variables on the stamping formability and investigate the effect of design variables on the quality characteristics of the product. Nguyen *et al.* [44] improved the press formability of a door hinge by changing the shape of the concerned area of the blank based on FE simulations. Furthermore, to improve the efficiency of sheet metal forming optimization, the meta-modeling technique is introduced. The meta-modeling technique is a method for replacing a complex model by an approximate one based on results calculated at various samples in the design space. Several meta-modeling techniques will be effective for the engineering optimization. These methods have been reviewed by Wang and Shan [45] in detail. See other literatures [46] and applications [48, 49] for further meta-modeling techniques. Accordingly, this application improves the door hinge press formability by changing the geometric shape of the die and bead punch in the concerned area. Fracture prediction using the finite element method is an easy and efficient way to apply ductile fracture criteria and determine the influence of changing the geometric parameters of the die and bead punch. In the near future studies, meta-modeling techniques will be applied to solve optimization problems in a certain design space and having certain constraints.

In this application, the forming process of a door hinge is simulated using ABAQUS/Explicit finite element code [32]. As the ductile failure criterion, the Oyane fracture criterion [50] via VUMAT user material based on a combined isotropic and kinematic hardening law is applied to improve the press formability of the door hinge. It is show to be a realistic and cost effective method. The FE simulation result for a cracked test sample are presented in Figure 3.2, where integral value I was calculated from the definition of the accumulated damage according to the Oyane ductile criterion.

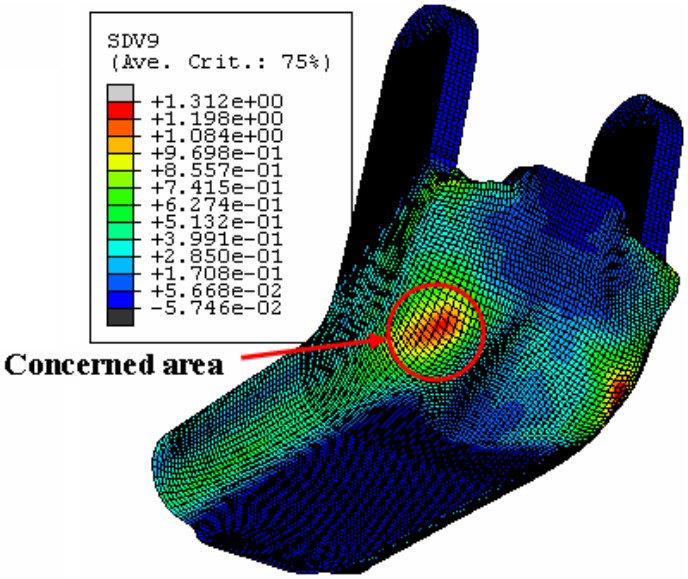

Figure 3.2: *Deformed shape in finite element simulation, where maximum of integral value I was 1.343 in concerned area*

The effect of the die and bead punch geometries are then investigated to determine their influence on the press formability and the results demonstrate the ability to predict when and where ductile damage will appear in the workpiece during the forming operation. Finally, the improved geometry is presented according to Taguchi's experimental technique to achieve the improved shape for the concerned area in the die and bead punch.

3.2 Finite element procedures

3.2.1 Materials

Table 3.1 shows the mechanical properties of the blank, SAPH-440 sheet steel with a thickness of 5mm. The parameters characterizing the uniaxial-stress-plastic-strain response of the material used in the FE simulations are also given in the Table in terms of the parameters in Swift's work-hardening law [51], using the following expression:

$$\bar{\sigma} = K(\varepsilon_0 + \bar{\varepsilon}_P)^n \quad (3.1)$$

Where K is the plastic coefficient, n is the work-hardening exponent, and $\bar{\sigma}, \bar{\varepsilon}_P, \varepsilon_0$ are the equivalent stress, equivalent strain, and yield strain, respectively.

Table 3.1: *Mechanical properties of tested material (SAPH-440)*

Material	SAPH-440
Density (ρ, kg/mm^3)	7.8e-09
Young's modulus (E, kN/mm^2)	210
Tensile strength (MPa)	380
ε_0	0.0078
K (MPa)	832.85
n-value	0.182

3.2.2 Ductile fracture criterion

Based on various hypotheses, certain criteria have already been proposed for ductile fractures [39, 52]. Oyane et al. [50] proposed a criterion allowing for the history of the hydrostatic stress affecting the occurrence of a ductile fracture, and this has been widely applied in the field of bulk forming with a high reliability [50, 52]. This criterion has also been used by Takuda et al. [53] to predict fracture initiation for the deep drawing processes of laminated composite sheets. The results were successful for the fracture prediction. Yet, it should be mentioned that the application of the ductile fracture criterion is more effective for low ductility materials. Thus, in the present study, the criterion of Oyane et al. [50] is employed in Equation (3.2):

$$\int_0^{\bar{\varepsilon}_f} \left(\frac{\sigma_m}{\bar{\sigma}} + C_1\right) d\bar{\varepsilon} = C_2 \quad (3.2)$$

where $\bar{\varepsilon}_f$ is the equivalent strain at which the fracture occurs, σ_m is the hydrostatic stress, $\bar{\sigma}$ is the equivalent stress, $\bar{\varepsilon}$ is the equivalent strain, and C_1, C_2 are the material constants.

To determine the material constants C_1, C_2 in Equation (2), destructive tests have to be operated under at least two types of stress conditions. Thus, the present study refers to the testing results of Ko et al. [54], where C_1, C_2 are simply determined by uniaxial and plane-strain tension tests [53]. The fracture strain for uniaxial tension and a plane strain state using a dome test was 0.7156 and 0.5686, respectively. From this result, the material constants C_1, and C_2 for the ductile fracture criterion were calculated as 1.9438, and 2.3831, respectively.

3.2.3 Combination of finite element simulation and criteria for ductile fracture

Figure 3.3 shows the finite-element model of ABAQUS version 6.5 for the forming test process. Here, the punch and die model were made from the shape of the product using CATIA software, the blank modeled using solid elements C3D8R, and the punch and die modeled using rigid surface-elements R3D4 with three integration points. Throughout this study, a uniform mesh was used for both the solid and rigid surface-elements. The average element size of the solid elements was about 1mm in width, 1mm in length, and 1mm in height. Meanwhile, the average element size of the rigid surface-elements was about 1 mm in width, and 1 mm in length.

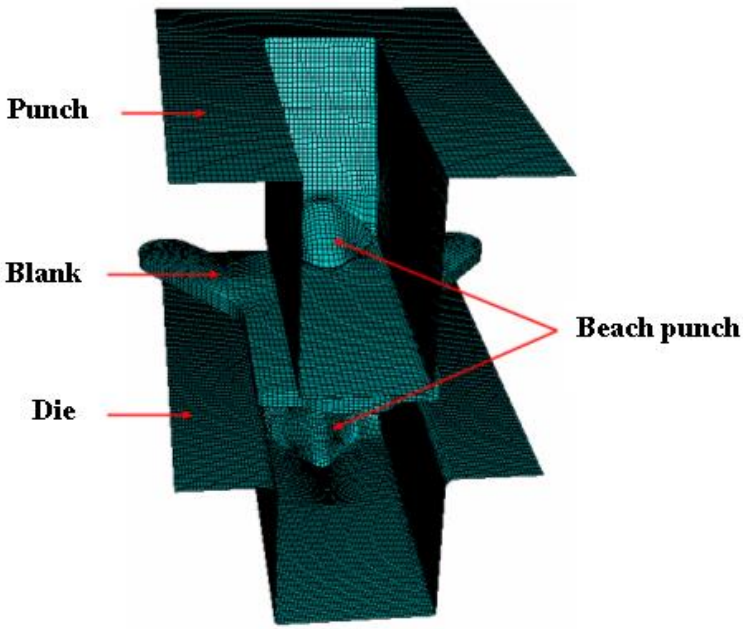

Figure 3.3: *Finite element model for test simulation*

The friction behavior of the blank-die/blank-punch was modeled using the Coulomb friction law. The friction coefficient μ_1 of the blank at the blank-die interface was measured using an automatic draw bead simulation [40], which was developed to simulate the friction state of a specimen under a drawing deformation mode. The test results revealed that the friction coefficient at the blank-die interface were within the range of μ_1=0.1 to 0.2. However, for the friction coefficient μ_2 at the blank/punch interface, μ_2=0.25, was assumed for all the simulations as in Reference [44].

In the simulation, for an elastic/plastic material with a combination of isotropic and kinematic hardening that obeys the von Mises yield criterion, the Equations (2.48-2.59) are valid if the strain rate and stress rate remain constant during a finite yet very small time increment $\underline{\Delta t}$.

The value for $\Delta\gamma$ of Equation (2.57) is used in the incremental Equation to determine σ_{new}, σ_{new}^{m}, and $\bar{\varepsilon}^{pl}$. These formulations are combined with the criterion of Oyane in Equation (3.2) and coded into a VUMAT subroutine, for use in ABAQUS/Explicit. When rewriting the criteria for a ductile fracture in Equation (3.2), the following integral is obtained:

$$I = \frac{1}{C_2}\int_0^{\bar{\varepsilon}_f}\left(\frac{\sigma_m}{\bar{\sigma}} + C_1\right)d\bar{\varepsilon} \qquad (3.3)$$

The histories of stress and strain in each element during forming are calculated using the FEM, and the ductile fracture integral *I* in Equation (3.3) is obtained for each element. When the integral value *I* of Equation (3.3) reaches 1.0, a fracture will occur. This ductile fracture value *I* can be calculated for every finite element during the forming process. Figure 3.4 shows the general updating flow-chart of the VUMAT subroutine implemented in ABAQUS.

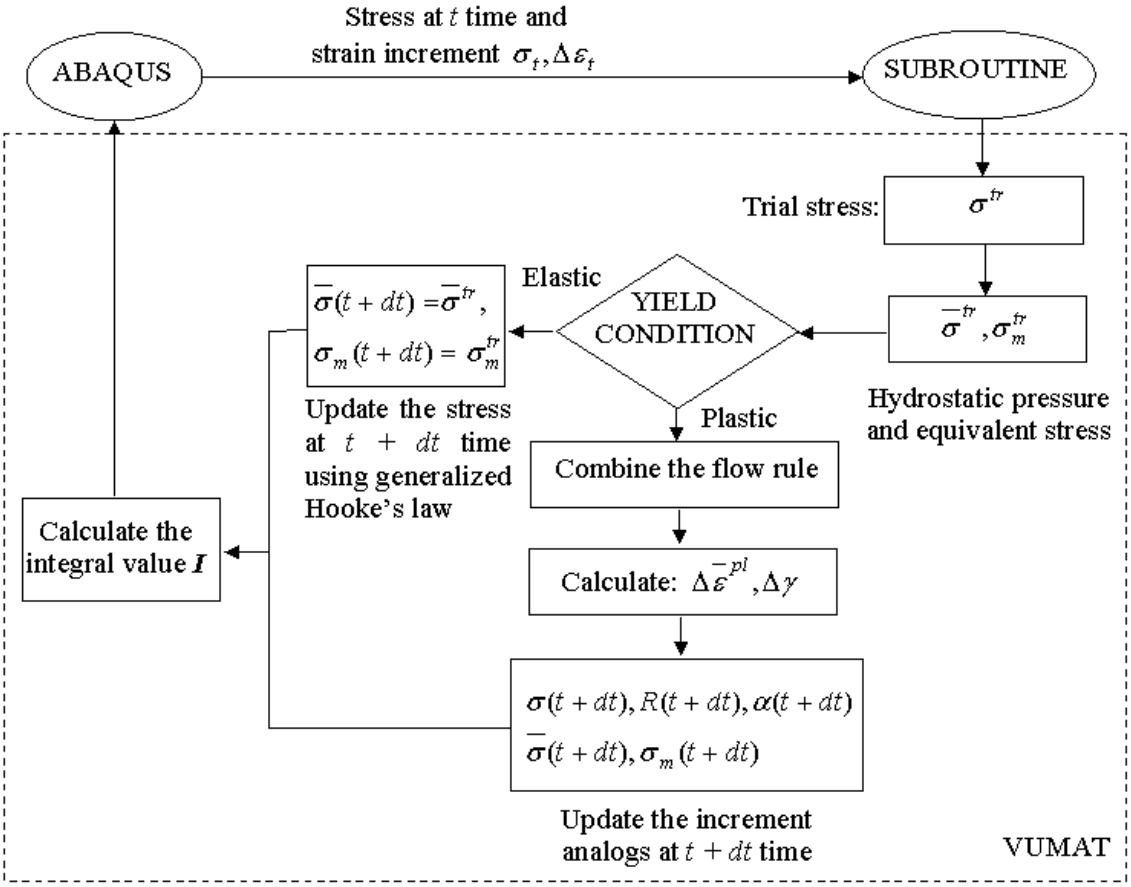

Figure 3.4: *The general updating flow-chart of subroutine*

3.3 Taguchi's Orthogonal Array

When manufacturing a door hinge manufacturing, fractures tend to occur near the punch corner of the blank. The reason for this is that the high tensile stress and equivalent plastic strain at the punch corner are larger than those in the other zones of the blank. When changing the geometry of the die and bead punch in the concerned area, it was found that the magnitude of the von-Mises stress and equivalent plastic strain were also changed. Therefore, the integral value *I* was changed. Thus, it was concluded that the geometry of the die and bead punch for the concerned area in the blank could be improved.

When using this characteristic, the problem becomes a smaller-the-better type problem according to the Taguchi method, which means the smaller the integral value *I,* the better the press formability.

The signal-to-noise ratio (S/N ratio) defined according to the Taguchi method is:

$$\eta_i(dB) = -10\, log_{10}(I^2) \tag{3.4}$$

where η denotes the observed value (unit: dB). Since the maximizing procedure for the S/N ratio minimizes the press formability, the best conditions can be obtained by maximizing (η_i). The factors to be considered here, to establish their effects on the press formability, are the die corner radius (R), the declination of the bead punch (a), and the peak angle of the bead punch (b).

Figure 3.5 presents the definition of these three factors, while their selected levels are listed in Table 3.2.

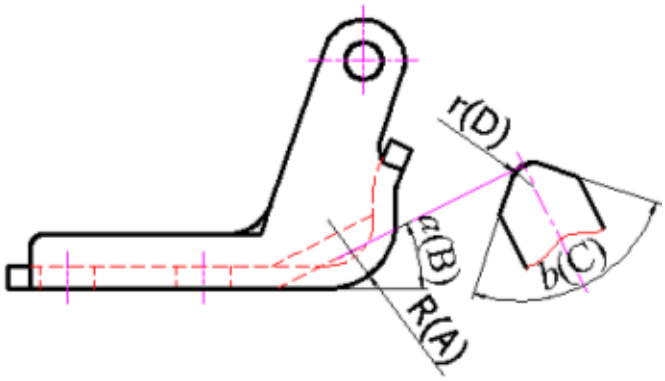

Figure 3.5: *Definition of factors in concerned area*

Table 3.2: *Factors and their levels in FEM simulation*

Factors	Level		
	1	2	3
A (R mm)	10	15	20
B (a^0)	14	22	30
C (b^0)	70	90	110

As the FE simulation using the three-level factors, an L_9 array can indeed be used to design the experiment. Therefore, a minimum of nine tests were required to investigate the effect on the FE simulation. Table 3.3 shows the L_9 orthogonal array chosen from Taguchi's standard-orthogonal-array Table. The number for each column is related to the level number for each factor. In this study, only the individual effects of each factor on the FE simulation were investigated, without considering the interactions between each factor.

Table 3.3: *Taguchi's L_9 orthogonal array for simulations*

Case	A (R mm)	B (a º)	C (b º)
1	1(10)	1(14)	1(70)
2	1(10)	2(22)	2(90)
3	1(10)	3(30)	3(110)
4	2(15)	1(14)	2(90)
5	2(15)	2(22)	3(110)
6	2(15)	3(30)	1(70)
7	3(20)	1(14)	3(110)
8	3(20)	2(22)	1(70)
9	3(20)	3(30)	2(90)

3.4 Results and Discussion

When the softening property is used in constitutive models, the stress-strain relation defined in FE simulation must be adjusted with respect to element size, keeping the fracture energy constant. This adjustment of the stress strain relation with the element size is a way of incorporating fracture mechanics theory into finite element computation. If all elements were given the same softening stress-strain relation regardless of element size, the result would be mesh-dependent due to the inconsistent fracture energy treatment. On the contrary, when the material property can be defined as plasticity, the redistribution of stresses can occur as a result of plastic flow. Failure is define as occurring when the entire material volume reaches simultaneous yielding. In such a case, the constitutive models can be made independent of the element size. In our research, after several times reduced the mesh size to carry out the Table and reliable FE simulation results, we used the average element size of the blank element was about 1mm in width, 1mm in length, and 1mm in height. This mesh size is small enough to analyze the plastic deformation and failure of door hinge. The FE simulation results for a cracked test sample with the von Mises stress $(\bar{\sigma})$, equivalent plastic strain $(\bar{\varepsilon})$, and the maximum ductile fracture value I (SDV9) calculated from Equation (3.3) via VUMAT user material based on isotropic hardening, kinematic hardening, and a combined isotropic/kinematic hardening law are presented in Figures 3.6(a), 3.6(b), and 3.6(c), respectively.

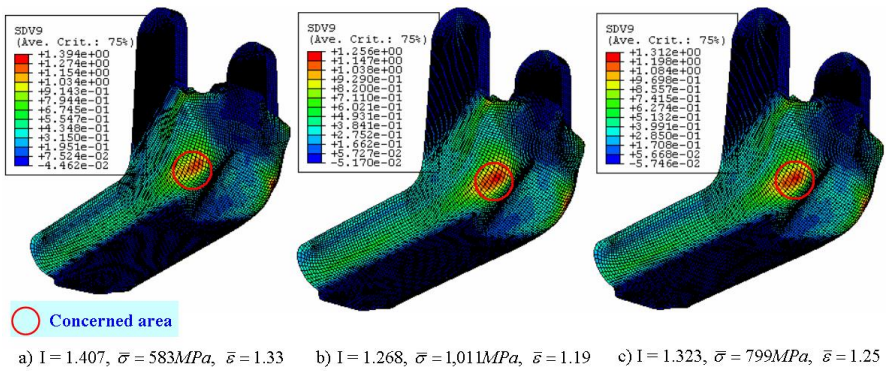

Figure 3.6: *Deformed shapes of product failure in finite element simulation based on (a) isotropic hardening, (b) kinematic hardening, and (c) combined isotropic/kinematic hardening law.*

The results show that the maximum ductile fracture values *I* were not so different, yet the maximum von Mises stresses $(\bar{\sigma})$ in the concerned area for all the three hardening models were distinctly different. From the combined isotropic/kinematic hardening law, the von Mises stress in the concerned area was closest to the equivalent stress of tensile failure. So, the combined isotropic/ kinematic hardening law will give better result when compared to other two hardening models. Figure 3.7 shows the evolutional stress state at the element having maximum value of ductile fracture value I in the concerned area with the combined isotropic/ kinematic hardening model for the case of R(A)=10mm, *a*(B)=30°, *b*(C)=90°, and r(D)=5mm.

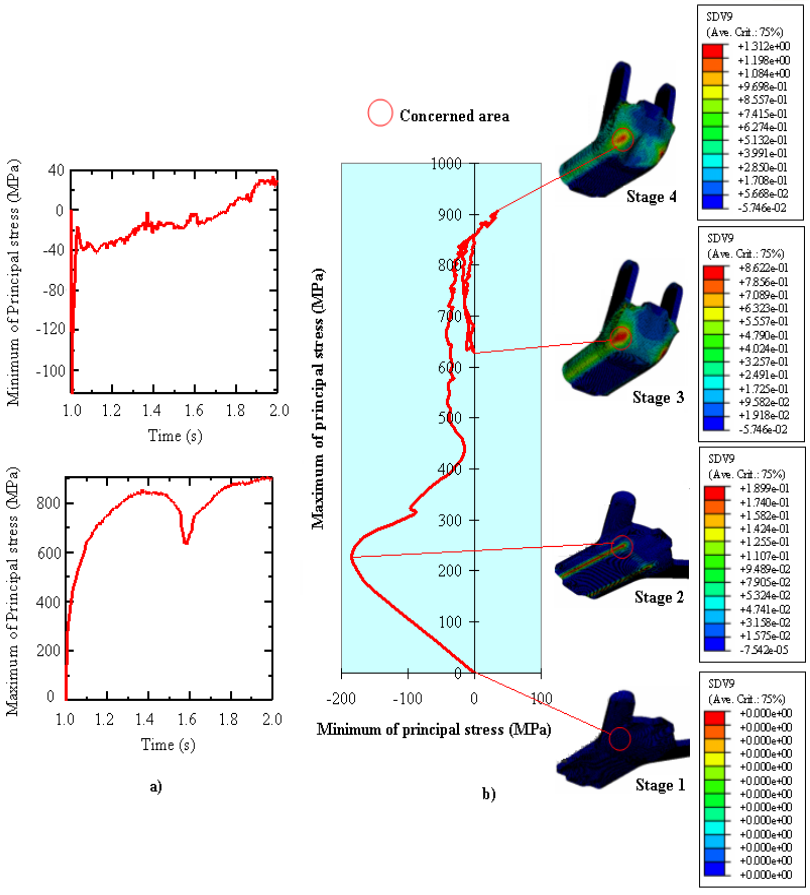

Figure 3.7: *Evolutional stress state in concerned area*

The evolutions of the maximum and minimum principal stress state at the element having maximum value of ductile fracture value I in the concerned area versus time are presented in Figure 3.7(a). Meanwhile, Figure 3.7(b) shows the stress path in the concerned area, which was complicated and also reversed between forming stage 2 and 3. Therefore, this complicated, reversed and nonlinear stress path in the concerned area supports the use of a combined isotropic/kinematic hardening law to predict the fracture of a door hinge.

In order to determine the scalar parameter β, the cyclic tensile curves, obtained by FE simulation via VUMAT user material through changing the values of β, was compared with experiment data and chosen the best fit as shown in Figure 3.8. The scalar parameter β for isotropic/kinematic hardening was estimated as 0.5.

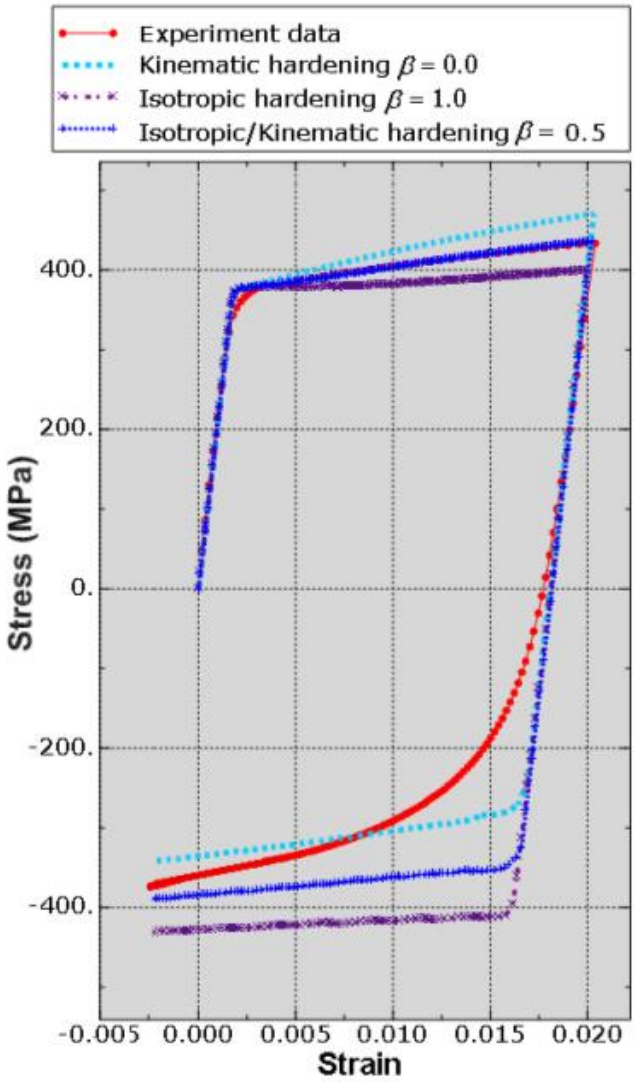

Figure 3.8: *Estimation of scalar parameter (β)*

Table 3.4 shows the results of the integral values I in numerical simulations based on a combined isotropic/kinematic hardening law for each case chosen from Taguchi's standard-orthogonal-array Table. The maximum value of the integral values *I*, i.e. the potential initial fracture site, appeared at the corner of the product for all cases. As mentioned before, the condition of failure was satisfied when and where the ductile fracture values *I* approached 1.0. For case no.2 and no.3, the ductile fracture values *I* were larger than 1.0, and failure appeared. The trends of the failure site predicted in this study were in good agreement with those in the actual product.

Table 3.4: *L_9 orthogonal array and calculated observed values*

Case	Column number and factor assignment				Ductile fracture value (I)	
	A (R)	B (*a*)	C (*b*)		I	η_i^a (dB)
1	1(10)	1(14)	1(70)		0.837	1.545
2	1(10)	2(22)	2(90)		1.007	-0.061
3	1(10)	3(30)	3(110)		1.343	-2.561
4	2(15)	1(14)	2(90)		0.815	1.777
5	2(15)	2(22)	3(110)		0.828	1.639
6	2(15)	3(30)	1(70)		0.843	1.483
7	3(20)	1(14)	3(110)		0.732	2.710
8	3(20)	2(22)	1(70)		0.743	2.580
9	3(20)	3(30)	2(90)		0.755	2.441

According to the Taguchi's method, an analysis of the mean (ANOM) and analysis of variance (ANOVA) were used to represent the relationship between the geometry factors for the concerned area and the observed values for the integral values *I*. In this experiment, the observed values were found to be related to the three parameters (Table 3.4). The optimization of the observed values was then determined through a comparison with the Taguchi signal-to-noise (S/N) ratio. The ANOVA values calculated for the three factors and their corresponding three levels (tabulated in Table 3.2) were obtained using an L_9 orthogonal array. The use of orthogonal array reduced the full factorial design down to 9 experiments from 81 experiments, thereby decreasing the cost, time, and effort. The increase in the factor effect was measured using the S/N ratio of the factors. Moreover, the analysis of the mean (ANOM) and analysis of variance (ANOVA) for the quality characteristics provided a better understanding of the individual effect of each factor. The ANOVA for the different factors - including the level average, total variation, sum of the squares, sum of the mean squares, and contribution - enabled various relative quality effects to be determined.

Tables 3.5 show a summary of the calculated results. The formulation used to calculate the sum of the squares was as follows:

$$3(m_{j1} - m)^2 + 3(m_{j2} - m)^2 + 3(m_{j3} - m)^2 \quad (3.5)$$

Where m is the overall mean of the η_i value for the four experiments, defined as $m = \frac{1}{9}\sum_{i=1}^{9}\eta_i = 1.284$, and m_{ji} is the average of η related to level *i (i=1, 2, 3)* of factor *j* given by $m_{ji} = \frac{1}{3}\sum_{i=1}^{3}(\eta_j)_i$.

The results of the ANOM and ANOVA for the ductile fracture values *I* (Table 3.5) revealed that the die corner radius (R), which reached 68.64%, made the major contribution to the overall performance. Meanwhile, the contribution percentages for the declination of the bead punch (*a*) and peak angle of the bead punch (*b*) were lower at 18.75% and 12.61%, respectively. The contribution percentage of the peak angle of bead punch (*b*) was the smallest at 12.61%. Thus, it was concluded that the die corner radius (R) factor had the most significant effect on the ductile fracture value *I* in the concerned area.

Table 3.5: *ANOM and ANOVA Table of effect on ductile fracture value (I)*

Factor	Average η by Level			Sum of Squares	D.O.F	Sum of mean squares	Contribution
	1	2	3				
A(R)	-0.359	1.633	2.577*	13.479	2	6.7395	0.6864
B(*a*)	2.011*	1.386	0.454	3.683	2	1.8415	0.1875
C(*b*)	1.869*	1.385	0.596	2.477	2	1.2385	0.1261
Total				19.639	6	9.8195	
* Indicates optimum level							

The η (dB) of the levels for each factor were individually calculated, as shown in Table 3.4. In the Taguchi method, the higher the η value, the better the overall performance, meaning that the factor levels with the highest η value should always be selected. Accordingly, the average for each experimental level was calculated using the highest η value for each factor to produce the response Table (Table 3.5). As shown in the response Table and response graph, the improved conditions to maintain the ductile fracture value *I* successfully in the forming test were $A_3B_1C_1$, which means R = 20 mm, *a* = 14°, *b* = 70°, and r = 5 mm. The S/N ratio for these improved conditions is denoted by η_{opt} and predicted as Equation (3.6):

$$\eta_{opt} = m + (m_{A3} - m) + (m_{B1} - m) = 3.304(dB) \quad (3.6)$$

Figure 3.9 depicts the FE simulation results of the improved conditions ($A_3B_1C_1$) for the press formability. Here, the equivalent stress, equivalent strain is decreased, and the integral value *I* has the minimum value. Figure 3.10 shows the experiment results for case No.8, where no crack appeared in the corner of the concerned area.

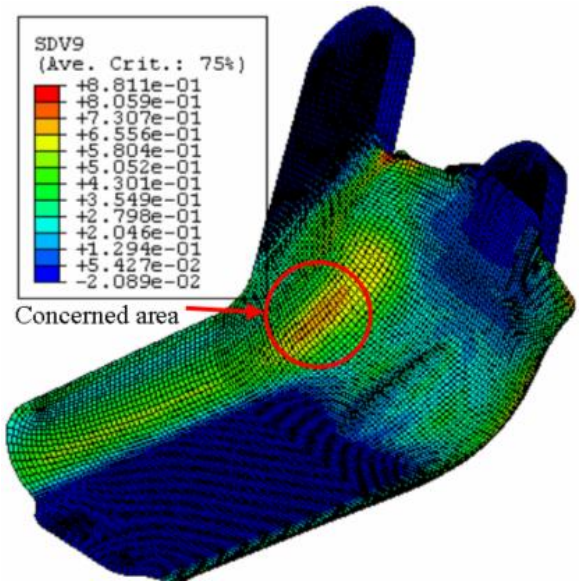

Figure 3.9: *Deformed shape in finite element simulation of optimum case, where integral value I was 0.725 in concerned area*

Figure 3.10: *Case No. 8: R=20mm, a=20º, b=90º, r=5mm, I=0.748. No crack occurred in concerned area*

From the above discussion, it was concluded that the use of Taguchi's experimental array for the FE simulations allowed successful improvement of the geometric shape of the die and bead punch in the concerned area to improve the press formability. As a result, the geometric shape of the die and bead punch in the area of concern was improved using a die corner radius (R) of 20 mm, declination of the bead punch (*a*) of 14^{o}, and peak angle of the bead punch (*b*) of 70^{o}.

3.5 Conclusion

To predict a fracture and improve the press formability of a door hinge, the geometric shape of the die and bead punch in the concerned area was improved using finite element simulations and then investigated by experiments. Commercial software (ABAQUS version 6.5, explicit formulation) with a user-defined subroutine (VUMAT) based on a combined isotropic/kinematic hardening model was used for the simulation according to the orthogonal array of Taguchi's method. As a result, the die corner radius (R) was identified as the important factor for improving the press formability of the door hinge. Improved geometric shapes for the die and bead punch in the concerned area, consisting of a die corner radius (R) of 20 mm, declination of the bead punch (*a*) of 14^{o}, and peak angle of the bead punch (*b*) of 70^{o}, were also predicted to produce a better reliability compared to the original test sample.

Chapter 4: Study of Incremental Sheet Forming for Complex Shape and its Improvement

4.1 Introduction

Incremental sheet forming (ISF) is an innovative process to manufacture sheet metal products by the (CNC) controlled movement of a simple forming tool which plastically deforms the blank according to the desired shape. The two main variations of incremental sheet forming are positive and negative forming. This refers to the side of the part that the tool works on. In negative forming the tool works on concave surface on the part, whereas in positive forming the tool moves on the convex surface. When the die has a positive geometry, the blank holder should be moved by hydraulic actuator in order to firmly maintain the sheet in proper working position; in the case of negative geometry, the blank can be fixed. Although it is a slow process, makes it a very suitable process for low series production, prototype manufacturing and complex components produced in small batches for aeronautical, automotive and medical applications due to the cost reduction linked to the fact that punches or dies are avoided, in comparison with the traditional stamping or drawing processes. This kind of process could go back to the conventional spinning process [55, 56] in which only axi-symmetric parts can be made. Besides, many other processes which can make both non-axi-symmetric parts as well as axi-symmetric parts have been developed. An incremental sheet forming process to make flanged sheet metal parts without dedicated tooling was developed by Powell *et al.* [57]. Matsubara [58] successfully formed various conic and pyramidal parts with the (NC) milling machine. Iseki and Kumon [59] have studied a forming limit for the incremental sheet forming process. They had shown that the forming limit curve (FLC) of sheet material in incremental sheet forming is located much higher than those based on theories of plastic instability. In order to investigate the influence of the main material parameters and process variables upon formability and improve the formability in incremental sheet forming several researches had been proposed [60, 61, 62**]**. Kim and Yang [63] proposed the double-forming technique to improve formability, assuming that only shear deformation occurs in the material. Recently, G. Hussain, and L. Gao *et al.* [64, 65, 66] presented an innovative method to test the thinning limits of sheet metals in negative incremental sheet forming along with verification of the

ISBN: 978-81-936820-9-8
Thesis DOI: 10.21467/books.75

Cosine's law of thickness distribution. They also showed that the formability in single point incremental sheet forming can be expressed as the maximum wall angle (θ_{max}). Besides, the effect of the curvature of a part's generatrix on the formability of an aluminum sheet has been investigated systematically to indicate that the formability increases as the radius of curvature decreases. Park *et al.* [67] studied and showed the possibility of cup incremental sheet forming of magnesium sheet at room temperature with rotational, where the tool rotates itself.

When manufacturing a complex shape by incremental forming, firstly a (CAD) file of the completed formed part must be designed, imported to (CAM) software, and simulated to generate the tool path or (CL) data file. Depending on the complexity of the part, the process can include a basic geometry supporting die or no dies at all. The tool path contours are then imported and performed on a standard (CNC) mill. For this kind of process in order to enhance the formability of sheet material in incremental sheet forming process, there are many process variables to be improved, such as the material properties, forming conditions, the shapes of the forming tool, curvature of part, dimension of forming part, specially down-step, offset tool path, and spindle speed also. These factors determine the formability, as regards the thickness variation, and blank failure after the incremental forming. As already pointed out in Ambrogio *et al.* [68] work, the single point incremental sheet forming process mainly depends on geometrical and process conditions. Particularly, the accuracy of the final geometry is mainly influenced by the tool down step.

Nowadays, numerical simulation is an essential tool for understanding of physical processes modelized by partial differential or integral Equations. After the pioneers work of finite-element method (FEM) for rigid-plastic FEM [69, 70, 71], elastic-plastic FEM [72, 73], (FEM) has been successfully applied to various kinds of sheet forming processes such as stamping [74, 75], hydroforming [75, 76], incremental sheet forming [68, 77, 78] etc., to clarify the forming characteristics, predict forming defect and improve the forming process. For incremental sheet forming the finite element analysis was also successfully used to study the effect of process variable on formability of materials in incremental sheet forming. In order to simulate incremental sheet forming by the finite element analysis, two different approaches could be pursued, namely an implicit model implementing a Lagrangian formulation or an explicit model. As shown by Ambrogio *et al.* [68] the use of explicit finite element simulation is a realistic and cost-effective method in predicting and investigating the effect of process variables on formability of incremental sheet metal forming. Several other studies were focused on the (FEM) analysis, taking into account simple shapes. Shim and Park [77] performed a numerical simulation of the single layer in the forming of truncated pyramid to find the deformation characteristics along the tool path. Iseki [78] simulated the incremental sheet forming of a shell of the frustum of a quadrangular pyramid. However, almost previous researches have focused on simple geometry models such as rectangular, circular geometries or the combination of both in simulation model.

In this study, the incremental sheet forming process for the product of complex geometry shape (e.g. human face) is studied using ABAQUS/Explicit finite element code and is improved using Taguchi's method. The input file was obtained by the combination of (CAM) and (CAE) simulation through using MATLAB programming. Figure 4.1(a) shows the tested sample in which failure occurred under improper forming conditions, the tool radius of 6 mm, the tool down-step of 2.0 mm, and the feed rate of 400 mm/min without rotating of the tool. The supported die is shown in Figure 4.1(b).

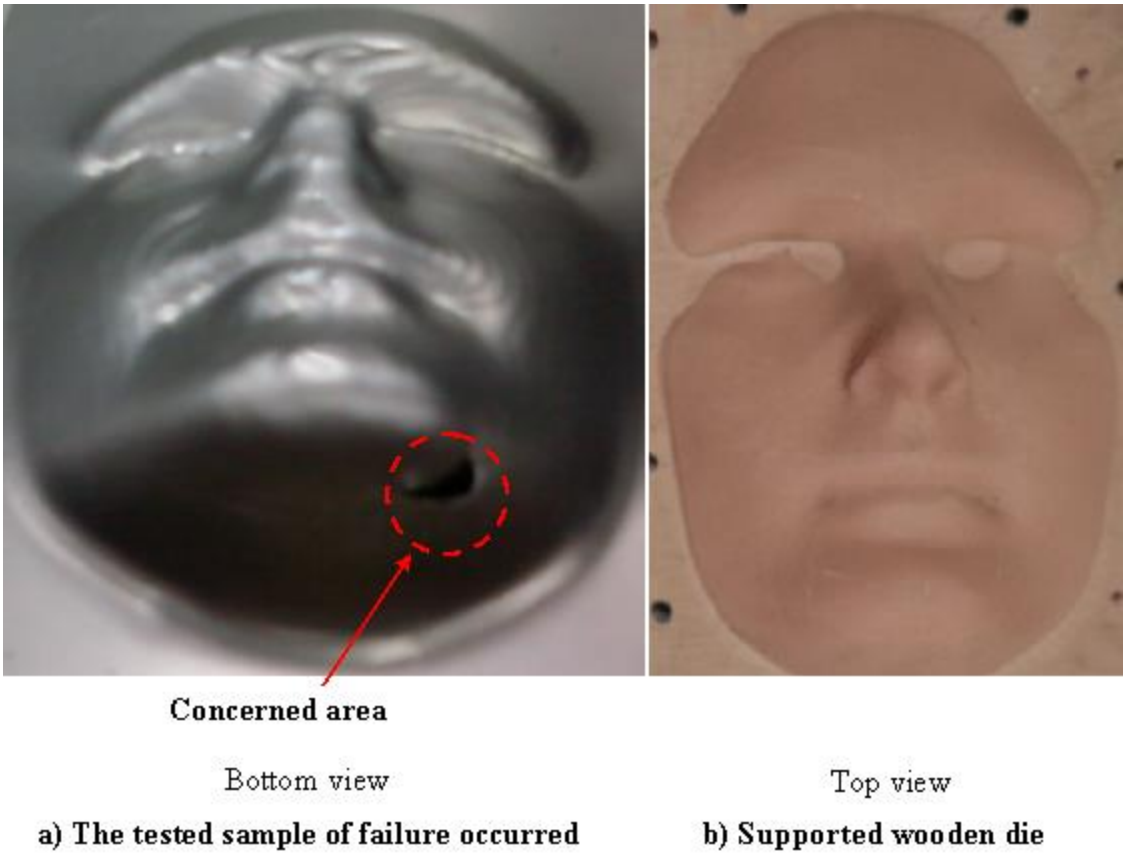

Figure 4.1: *Deformed shapes in experiment of failure test sample.*

Figure 4.2 depicts (FEM) simulation results for tested sample. The effects of forming variables, such as tool radius, tool down-step, friction coefficient, etc. are then investigated to determine their influence on the formability by comparing with forming limit curve. Taguchi's experimental technique is adopted to achieve the improved condition of these process variables.

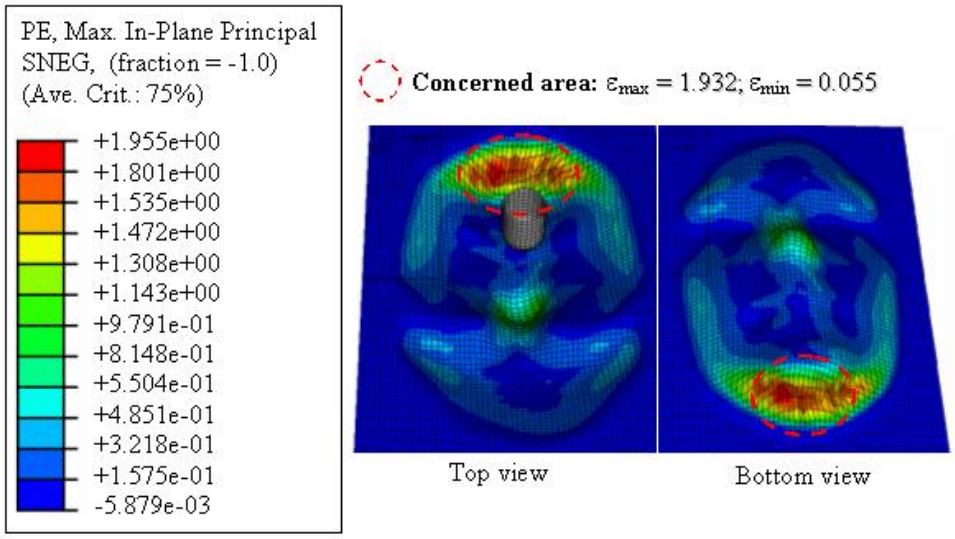

(a)

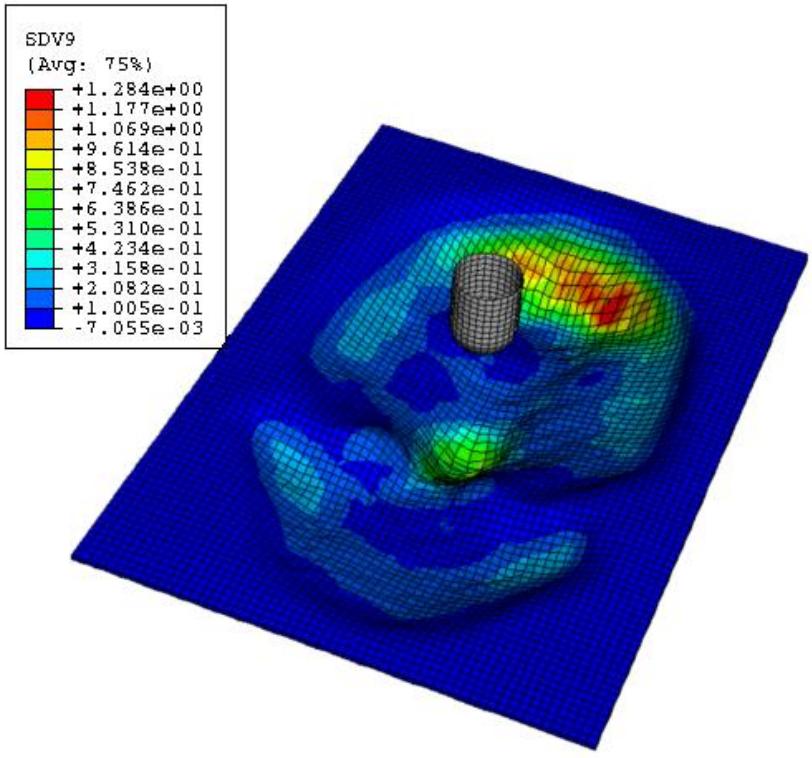

(b)

Figure 4.2: *The FE simulations for a failure test sample.*

4.2 Finite Element Simulation

This study used the commercial software ABAQUS version 6.5-1 to simulate the forming process. This software can provide elastic-plastic and rigid-plastic simulations of metal forming in the case of a large deformation, thereby significantly reducing the cost and time involved in tool and die design.

The flow pattern, equivalent stress distribution, equivalent strain distribution, and major and minor strains can all be simulated by (FEM). These simulation results can then be used to obtain the product geometric profile and material properties required. In the pre-process of modeling metal forming, the 3D mechanical type, geometric profile of the blank, and contact surfaces are constructed using the (GUI) of ABAQUS version 6.5-1. An elastic-plastic model is then selected and the material properties, such as Young's modulus, Poisson's ratio, and the density, are needed. The anisotropic work-hardening rule is applied in the flow rule due to plastic strain hardening. The changes in the Von-Mises stress, major and minor strains yielded on the surface are plotted. The initial conditions of the components are set-up, and the contact between the blank, punch, and die is defined.

4.2.1 Geometry and FE models

Figure 4.3 shows the finite-element model for the incremental sheet forming test process. Here, the tool and die model were made from the shape of the product using CATIA software, the blank modeled using both of shell elements S4R without VUMAT subroutine and solid elements C3D8R via VUMAT user material, and the punch and die modeled using rigid surface-elements R3D4. Throughout this study, the average element size of the blank and rigid tool was about 1 mm in width, and 1 mm in length; the average element size of the rigid die was about 2 mm in width, and 2 mm in length.

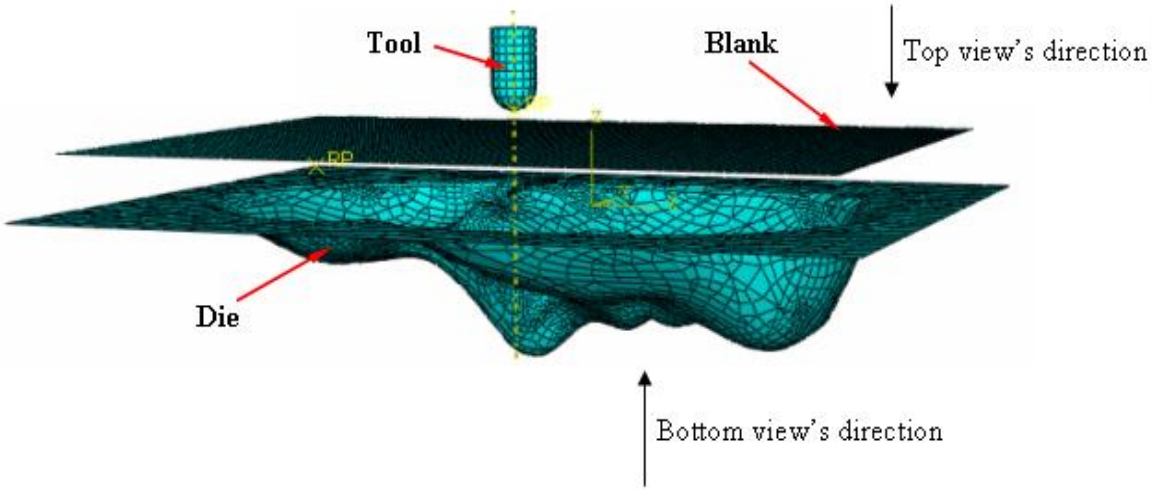

Figure 4.3 *Finite element model for simulation.*

4.2.2 Materials

Table 4.1 shows the mechanical properties of the blank, a cold rolled steel. The parameters characterizing the uniaxial-stress-plastic-strain response of the material used in the (FE) simulations are also given in the Table in terms of the parameters in Swift's work-hardening law, using the expression of Equation (3.1).

Table 4.1: *Mechanical properties of tested material (Cold Rolled Steel)*

Material	Cold Rolled Steel
Density (ρ)	7.8e-06
Young's modulus (E)	210
Possion's ratio	0.3
Tensile strength (MPa)	140
ε_0	0.0009
K (MPa)	534.1
n-value	0.274
Lankford value R_m	1.679

4.2.3 Boundary conditions, loading, and interactions

The die was fixed in all directions. The tool was allowed to move following the tool-path which was obtained from (CAM) simulation. The friction behavior was modeled using the Coulomb friction law. The friction coefficient μ_1 between the blank and the punch is assumed to be the same as the fiction coefficient μ_2 between the blank and the die.

4.2.4 Ductile fracture criterion

In order to predict the failure of the incremental forming for complex shape the criterion of Oyane is employed as Equation (3.2), Here, C_1, C_2 are simply determined by uniaxial and plane-strain tension tests [24]. The material constants C_1, and C_2 for the ductile fracture criterion were calculated as 0.15, and 0.76, respectively.

4.3 Obtained CAE input file procedures

4.3.1 Tool path generation

In order to obtain cutter location (CL) data for human surface, (3D) scanner is used to create a point cloud of geometric samples on the surface of the object. These points can be used to extrapolate the shape of the object. Normally, the point clouds produced by (3D) scanners will not be used directly. Mostly all the applications using polygonal (3D) models, (NURBS) surface models, or ediTable feature-based (CAD) models. The process of converting a point cloud into a (3D) model in any forms described above is called 'reconstruction or "modeling"'.

Therefore, the reconstruction and modification is performed by utilizing CATIA software to creat (NURBS) surface model from point cloud and scale down as 65% in order to fit with small experimental machine. After having (CAD) model, we proposed two methods to obtain (CL) data and simulation process as shown in Figure 4.4.

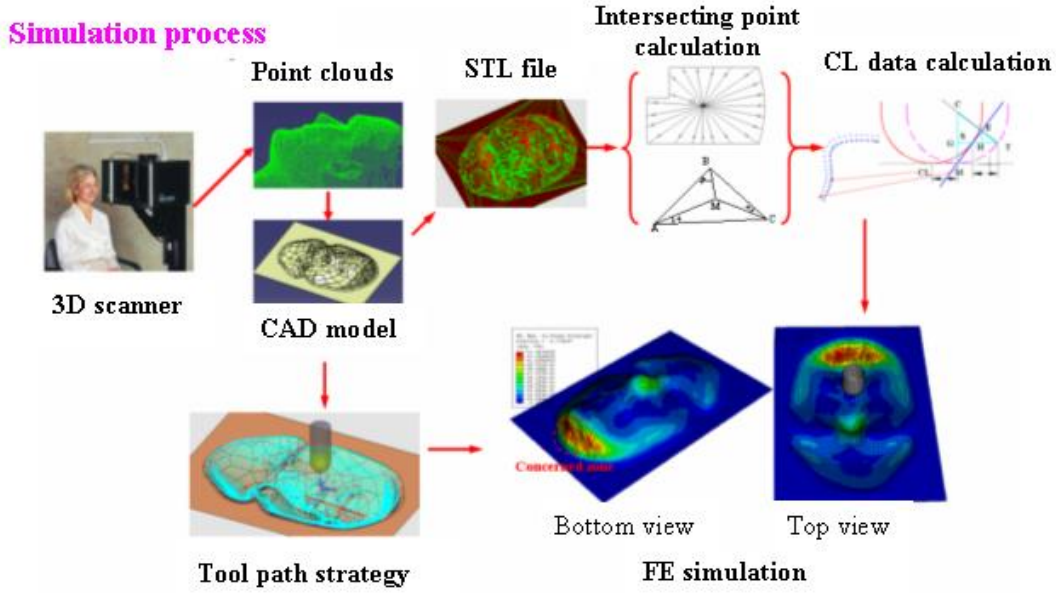

Figure 4.4: *The method to obtain CL data and simulation process.*

The first method is a basic programming method by using MALAB software. Following this method, initially the (CAD) model was saved to STL (standard triangulation language) file which consists of an unordered list of triangular facets representing the outside surface of the object. These triangular facets are described by a set of *X*, *Y* and *Z* co-ordinates for each of the three vertices and a unit normal vector with *X*, *Y* and *Z*. In order to generate inside intersection points of triangular which will be used to calculate cutter location (CL) at each Z layer of tool down-step, we first projected *n* divisions following radial direction from center axis and calculated intersection points of projection line and the planes containing three vertices of triangular. The intersection points must be then verified whether the points are insides or outsides of triangular as shown in Figure 4.5 in order to get all insides.

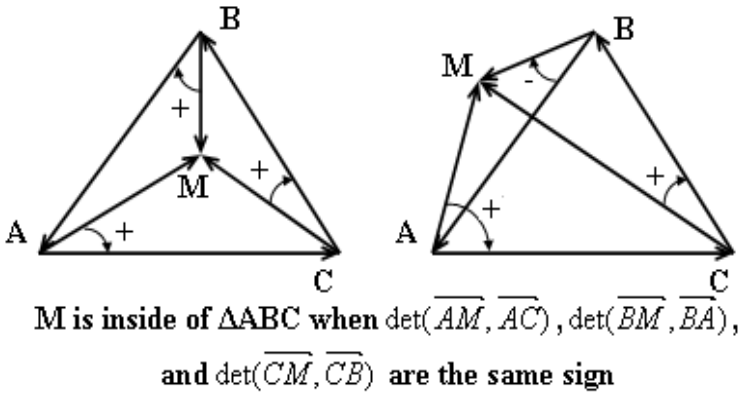

Figure 4.5: *Verification of the intersection points.*

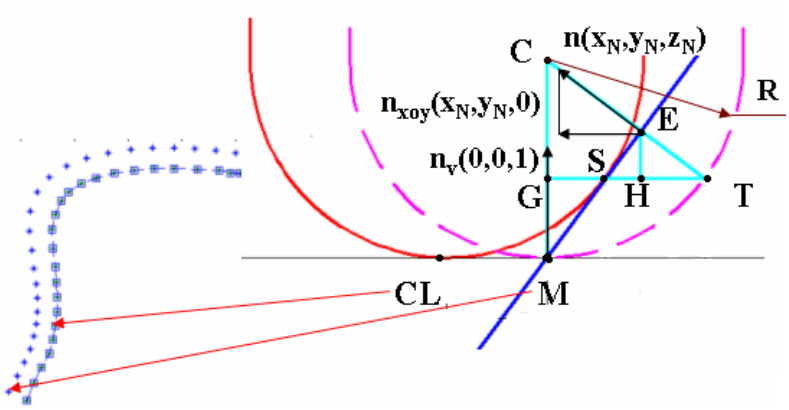

Figure 4.6: *Calculation of cutter location (CL) points.*

Finally, as depicted in Figure 4.6 from inside intersection points we can calculate (CL) points following listed Equations:

$$c = m + Rn_v$$

$$t = c - Rn_n$$

$$|CE| = |CG| = |Rn_v n_n|$$

$$e = c - |CE|n_n$$

$$|ET| = |E - T|$$

$$h = e - |ET|n_v$$

$$|ST| = \frac{(|ET|)^2}{|HT|}$$

$$cl = m + |ST|n_{xoy} \tag{4.1}$$

where *c, m, t, e, h, cl* are vectors corresponding to the tip points *C, M, T, E, H, CL*; R is tool radius; n_n is unit normal vector of triangular; n_v is unit vertical vector; n_{xoy} is the projective vector of n_n into xoy plane.

We also proposed a second method to obtain (CL) data from utilizing (CAM) software. Here, the (CAD) model was saved to (IGES) file and import to (CAM) software, namely CIMATRON E 6.0, that are used to generate (CL) data and also define the motion of the machines during processing. In this software, a Z-level milling operation is selected with spiral

tool path strategy and out-in downward movement of the tool (Figure 4.7). After simulation, the (CL) file, which includes the position of tool center point followed linear and circular interpolation, is generated and used to modify (CAE) input file.

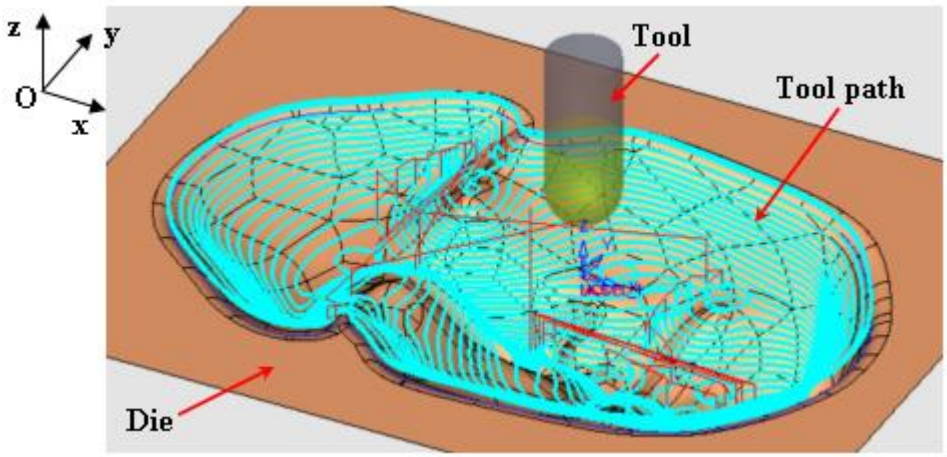

Figure 4.7: *Tool path strategy.*

4.3.2 CAE input file modifications

As mention in the second method, (CL) file includes linear and circular interpolations of the position of tool center point. Linear interpolations are easy to assign the forming tool movement in ABAQUS. But in circular interpolations, tool center point must be rotated around the other center points generated by (CAM) sofware, and it seems impossible to assign the forming tool movement in ABAQUS. So that in this study, a procedure has been completed, which scans the circular interpolations and divides them into linear segments satisfying allowable error.

By using ABAQUS, the forming tool movements are defined through the step module. It means that the movements are correlative with the steps of step module. Fortunately, there are more than thousand steps needed to simulate in incremental sheet forming process. If we operate the position of tool center point manually, it will take a lot of time and may be a chance of getting some manual error. So in this study, MATLAB software has been used as a programming tool to modify the (CL) data and also (CAE) input file.

Because the procedures for other steps are similar except values of position coordinates of tool center point. So firstly, the (CAE) input file is exported to get initial (CAE) input file. Then the text file of (CL) data is modified to obtain all position coordinate of tool center point as a standard (CL) data file through a subroutine of MALAB. Finally, in order to obtain final (CAE) input file, another MATLAB's subroutine had been written to add all next steps and assign values of tool center point from the standard (CL) data file to initial (CAE) input file for the correlative steps

4.4 Taguchi's Orthogonal Array

As above mentioned, many process variables contribute to enhancing the formability of incremental sheet forming process. If process variables are not suitably selected, a failure will appear at the concerned area. In this study, tool radius (*R*), tool down step (*H*), and the friction coefficient (μ) are considered as main process variables which govern the formability of material in incremental sheet forming. Thus, we try to verify and improve their influences on formability. For this kind of process, the failure was subjected to serious strain during the incremental sheet forming and found to be prone to internal or superficial micro-defects due to excessive tensile stress This initial damage and its growth then cause quality problems, such as necking and fractures, due to ductile tearing of the sheet. The reasons are that the high tensile stress and equivalent plastic strain at this area are larger than those in the other zones of the blank or the small difference between the major strains (ε_1) and the (FLC) values at the same point for the minor strains (ε_2) at the concerned area, (Figure 4.8)$(\Delta\varepsilon = \varepsilon_{FLC} - \varepsilon_1)$. The forming limit curve (FLC) in incremental sheet forming will be estimated and explained in more detail in Section 5. When changing the process variables, it was found that the magnitude of the difference in the major strain $(\Delta\varepsilon)$ and the integral value *I* also changed. Thus, it was concluded that the forming conditions of the product in incremental sheet forming could be improved.

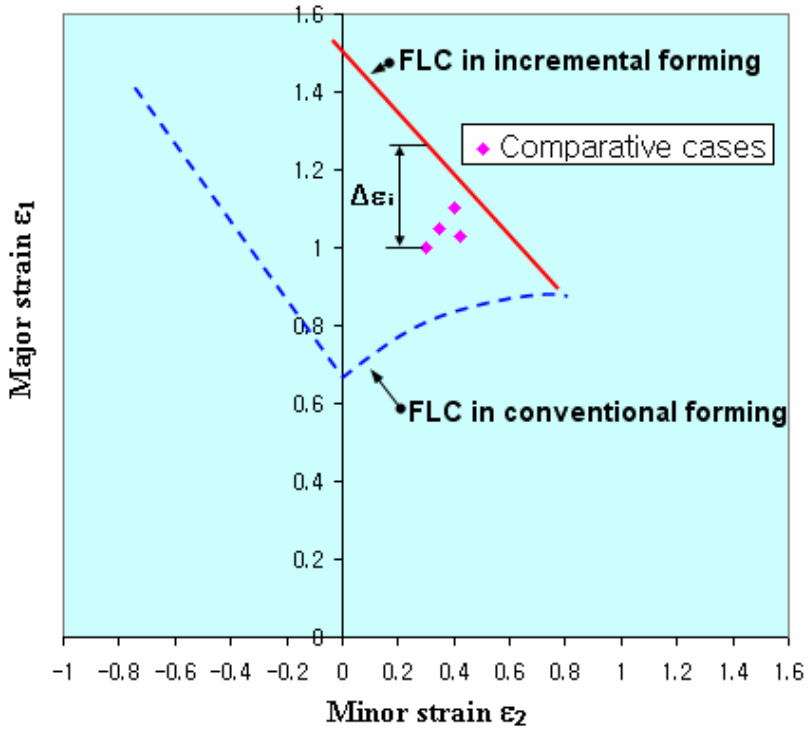

Figure 4.8: *Definition of the difference of major strain (Δε).*

In the preliminary study, the difference in the major strain$(\Delta\varepsilon)$ and the integral value *I* were set as the objective functions of the incremental sheet forming process. An analysis of the selected objective characteristics and values of the difference in the major strain$(\Delta\varepsilon)$ and the integral value *I* allowed the level of deviation to be calculated to identify which process variables were significant for the experiment.

When using this quality characteristic, the problem becomes a larger-the-better type problem in the case of the difference in the major strain$(\Delta\varepsilon)$ and smaller-the-better type problem in the case of ductile fracture criterion. Thus, according to the Taguchi method, the larger the difference in the major strain$(\Delta\varepsilon)$ and the smaller the integral value *I*, the better the incremental sheet forming process.

The signal-to-noise ratio (*S*/*N* ratio) defined according to the Taguchi method is:

$$\eta_i^1 = -10\, log_{10}(\Delta\varepsilon^{-2}) \tag{4.2a}$$

$$\eta_i^2 = -10\, log_{10}(I^2) \tag{4.2b}$$

Where η denotes the observed value (unit: dB). Since the maximizing procedure for the S/N ratio minimizes the press formability, the best conditions for the incremental sheet forming process can be obtained by maximizing (η_i)

Figure 4.9 presents the definition of the three defined process variables, while their selected levels are listed in Table 4.2.

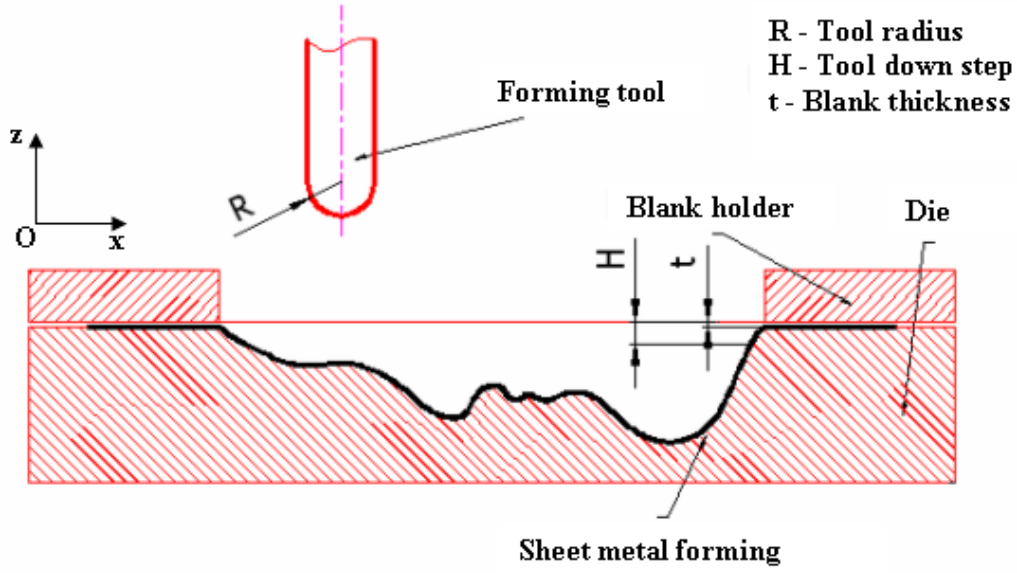

Figure 4.9: *Definition of considering parameters.*

Table 4.2: *Factors and their levels in FEM simulation*

Factors	Level		
	1	2	3
A (*R* mm)	6	5	4
B (*H* mm)	1.4	1.0	0.7
C (μ)	0.20	0.15	0.10
D (*t* mm)	1.0	1.0	1.0

As the FE simulation using the three factors with three levels gave nine degrees of freedom, a minimum of nine tests were required to investigate the effect on the FE simulation. Table 4.3 shows the L_9 orthogonal array chosen from Taguchi's standard-orthogonal-array Table. The number for each column is related to the level number for each factor. In this study, only the individual effects of each factor on the (FE) simulation were investigated, without considering the interactions between each factor.

Table 4.3: *Taguchi's L9 orthogonal array for simulations*

Case	A (*R* mm)	B (*H* mm)	C (μ)	D (*t* mm)
1	1(6)	1(1.4)	1(0.20)	1(1.0)
2	1(6)	2(1.0)	2(0.15)	1(1.0)
3	1(6)	3(0.7)	3(0.10)	1(1.0)
4	2(5)	1(1.4)	2(0.15)	1(1.0)
5	2(5)	2(1.0)	3(0.10)	1(1.0)
6	2(5)	3(0.7)	1(0.20)	1(1.5)
7	3(4)	1(1.4)	3(0.10)	1(1.0)
8	3(4)	2(1.0)	1(0.20)	1(1.0)
9	3(4)	3(0.7)	2(0.15)	1(1.0)

4.5 Estimation of FLC in incremental SHEET forming

To estimate the forming limit curve of the sheet, some conclusions from the previous researchers have been mentioned as follows:

- Swift's diffused necking criterion [51] for thin sheets and Hill's localized necking criterion [79] associated with the Hill's quadratic yield function [80] are used to construct the (FLC) in conventional forming (FLC at necking: FLCN) for the bi-axial tensile strain zone and tensile–compressive strain zone, respectively. So by using power law Equation (3.1), forming limit curve can be derived based on in-plane test (M-K model).

- From the previous literature [59, 77], most forming limit curves in incremental sheet forming (FLC at fracture: FLCF) appears to be a straight line with a negative slope in the positive region of the minor strain.

However, as a pointed out by several authors [81, 82] both of (FLCN) and (FLCF) curves at equi-biaxial strain nearly converge at one point. Thus, in the present study, the criterion of Clift et al [83] is employed in Equation (4.3) in order to calculate others points of (FLCF) in incremental sheet forming through the relationship of major/minor strain Equation (4.4), and the equivalent strain function for plane stress Equation (4.5) .

$$\int_0^{\bar{\varepsilon}_f} \bar{\sigma}\, d\bar{\varepsilon} = C \tag{4.3}$$

$$\beta = \frac{\varepsilon_2}{\varepsilon_1} \tag{4.4}$$

$$\bar{\varepsilon} = \frac{R_m+1}{\sqrt{2R_m+1}} \sqrt{1 + \frac{2R_m}{R_m+1}\beta + \beta^2}\,\varepsilon_1 \tag{4.5}$$

where $\bar{\varepsilon}_f$ is the equivalent strain at which the fracture occurs, $\bar{\sigma}$ is the equivalent stress, $\bar{\varepsilon}$ is the equivalent strain, C is the material constant, β is strain ratio, R_m is Lankford value, and ε_1, ε_2 are minor and major strains respectively.

After substituting power law Equation (3.1) into ductile fracture criterion Equation (4.3) and executing integral calculus we can derive the equivalent strain at the ductile fracture as a constant value Equation (4.6)

$$\bar{\varepsilon}_f = C_1 \tag{4.6}$$

To determine C_1 the values of strain ratio and major strain at equi-biaxial are used. The prediction of forming limits with the characteristic factors affecting the shape and level of the forming limits were implemented utilizing the algorithm developed by Son and Kim [84]. At equi-biaxial, the strain ratio β is 1.0, and the fracture major strains for the cases of tool radius R = 6 mm, R = 5 mm, and R = 4 mm was 0.98, 1.03 and 1.12, respectively. From this result, the constant values C_1 for the case of radius tool R = 6 mm, R = 5 mm and R = 4 mm were calculated as 2.27, 2.39 and 2.59, respectively. Finally, as depict in Figure 4.10, other points of (FLC) in incremental sheet forming were obtained by using various values of strain ratios and substituting into Equations (4.4), (4.5), and (4.6).

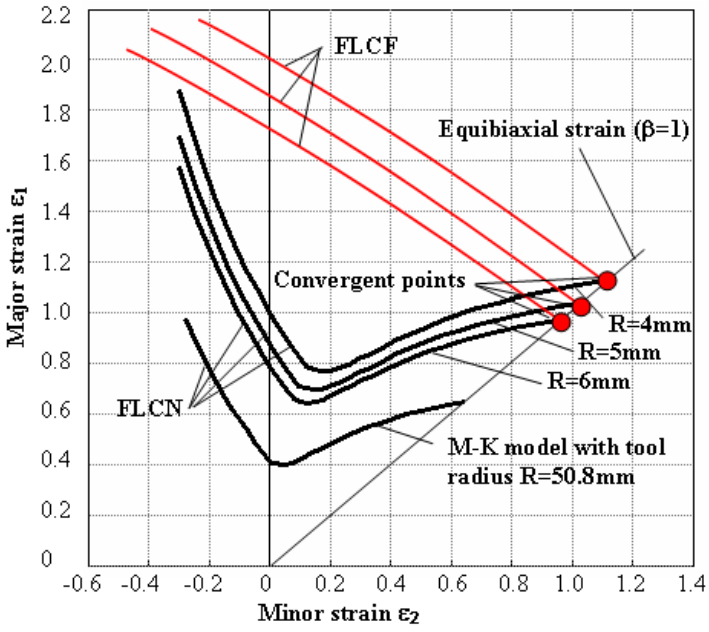

Figure 4.10: *Obtainment of FLC in incremental forming.*

4.6 Results and Discussion

In order to determine the scalar parameter β, the tensile curves, obtained by FE simulation via VUMAT user material through changing the values of β, was compared with the stress -strain experiment data which obtained from uniaxial tension test and then chosen the best fit. The scalar parameter β for isotropic/kinematic hardening was chosen as 0.65 as showed in Figure 4.11.

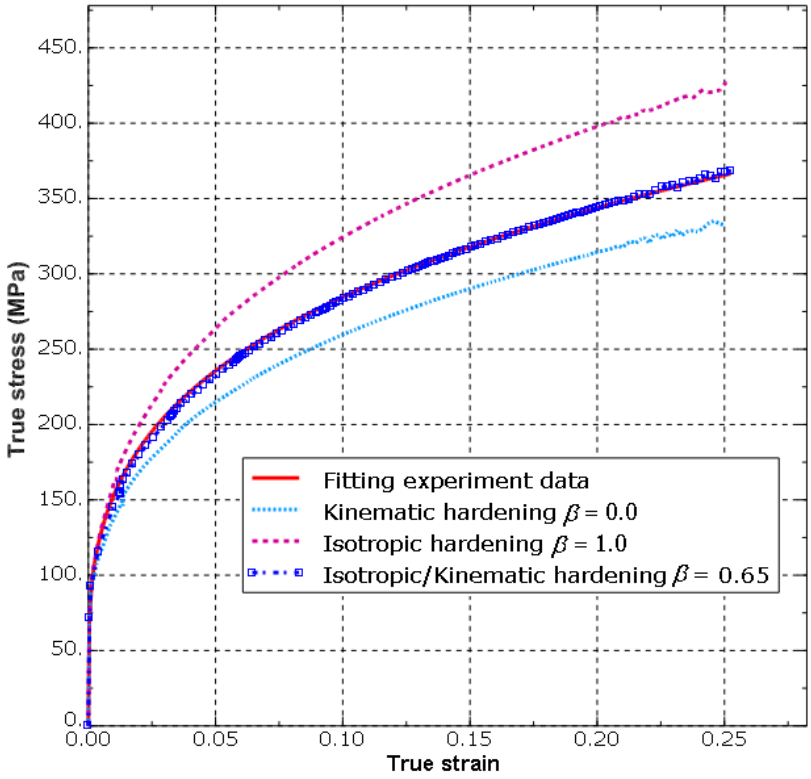

Figure 4.11: *Estimation of scalar parameter (β).*

Table 4.4 shows the results of the difference in the major strain$(\Delta\varepsilon)$ and the integral values I in numerical simulations based on a combined isotropic/kinematic hardening law for each case chosen from Taguchi's standard-orthogonal-array Table. The maximum value of the integral values *I* and minimum value of the difference in the major strain$(\Delta\varepsilon)$, i.e. the potential initial fracture site, appeared at the corner with large depth and slope angle value of the product for all cases. As mentioned before, the condition of failure was satisfied when and where the ductile fracture values *I* approached 1.0. For case no.2 and no.3, the ductile fracture values *I* were larger than 1.0, and failure appeared. The trends of the failure site predicted in this study were in good agreement with those in the actual product.

Table 4.4: *L_9 orthogonal array and calculated observed values*

Case	Column number and factor assignment			Ductile fracture value (I)		Difference in major strain ($\Delta\varepsilon$)	
	A (R mm)	B (H mm)	C (μ)	I	η_i^a (dB)	$\Delta\varepsilon$	η_i^b (dB)
1	1(6)	1(1.4)	1(0.20)	1.285	-2.178	-0.025	-32.041
2	1(6)	2(1.0)	2(0.15)	1.156	-1.259	0.115	-18.786
3	1(6)	3(0.7)	3(0.10)	1.054	-0.457	0.231	-12.729
4	2(5)	1(1.4)	2(0.15)	1.201	-1.591	0.061	-24.293
5	2(5)	2(1.0)	3(0.10)	1.078	-0.652	0.179	-14.943
6	2(5)	3(0.7)	1(0.20)	0.982	0.158	0.302	-10.400
7	3(4)	1(1.4)	3(0.10)	1.067	-0.563	0.197	-14.111
8	3(4)	2(1.0)	1(0.20)	1.031	-0.265	0.275	-11.213
9	3(4)	3(0.7)	2(0.15)	0.934	0.593	0.363	-8.802

According to the Taguchi method, an analysis of the mean (ANOM) and analysis of variance (ANOVA) were used to represent the relationship between the geometry factors for the concerned area and the observed values for the difference in the major strain$(\Delta\varepsilon)$ and ductile fracture value *I*. In this experiment, the observed values were found to be related to the three process variables (Table 4.4). The improvement of the observed values was then determined through a comparison with the Taguchi signal-to-noise (S/N) ratio. The (ANOVA) values calculated for the three factors and their corresponding three levels (tabulated in Table 4.2) were obtained using an L_9 orthogonal array. The use of orthogonal array reduced the full factorial design down to 9 experiments from 81 experiments, thereby decreasing the cost, time, and effort. The increase in the factor effect was measured using the S/N ratio of the factors. Moreover, the analysis of the mean (ANOM) and analysis of variance (ANOVA) for the quality characteristics provided a better understanding of the individual effect of each factor. The (ANOVA) for the different factors - including the level average, total variation, sum of the squares, sum of the mean squares, and contribution - enabled various relative quality effects to be determined. Table 4.5 shows a summary of the calculated results.

Table 4.5: *ANOM and ANOVA Table for effect of difference in major strain*$(\Delta\varepsilon)$

Factor	Average η by Level			Sum of Squares	D.O.F	Sum of mean squares	Contribution
	1	2	3				
A(R)	-21.185	-16.545	-11.375*	144.486	2	72.243	0.338
B(H)	-23.482	-14.981	-10.643*	255.911	2	127.9555	0.598
C(μ)	-17.885	-17.294	-13.927*	27.347**	2	13.6735	0.064
Total				427.744	6	213.872	
* Indicates the optimum level ** Indicates the sum of squares added to estimate the pooled error sum of squares in parentheses							

The formulation used to calculate the sum of the squares was as follows:

$$3(m_{j1} - m)^2 + 3(m_{j2} - m)^2 + 3(m_{j3} - m)^2 \quad (4.7)$$

Where m is the overall mean of the η_i, value for the nine experiments, defined as $m_1 = 1/9\sum_{i=1}^{9}\eta_i^2 = -16.369, m_2 = 1/9\sum_{i=1}^{9}\eta_i^2 = -0.691$ and m_{ji} is the average of η related to level i $(i=1, 2, 3)$ of factor j given by $m_{ji} = 1/3\sum_{i=1}^{3}(\eta_j)_i$.

The results of the ANOM and ANOVA for the difference in the major strain$(\Delta\varepsilon)$ and ductile fracture value I (Table 4.5 and 4.6) revealed that the tool down-step (H), which reached 59.83% (Table 4.5) (60.72% (Table 4.6)), made the major contribution to the overall performance. Meanwhile, the contribution percentages for the tool radius (R) and friction coefficient (μ) were lower at 33.78% (Table 4.5) (37.92% (Table 4.6)) and 6.39% (Table 4.5) (1.69% (Table 4.6)), respectively. The contribution percentage of the friction coefficient (μ) was the smallest. Thus, it was concluded that the tool down-step (H) factor had the most significant effect on the press formability in the area of concern, while the effect of the friction coefficient (μ) was negligible.

Table 4.6: *ANOM and ANOVA Table of effect on ductile fracture value (I).*

Factor	Average η by Level			Sum of Squares	D.O.F	Sum of mean squares	Contribution
	1	2	3				
A(R)	-1.298	-0.695	-0.078*	2.231	2	1.1155	0.3792
B(H)	-1.444	-0.726	0.098*	3.573	2	1.7865	0.6072
C(t)	-0.762	-0.752	-0.557*	0.080	2	0.0400	0.0136
Total				5.884	6	2.942	
* Indicates optimum level ** Indicates sum of squares added to estimate pooled error sum of squares in parentheses							

The η (dB) of the levels for each factor were individually calculated, as shown in Table 4.4. In the Taguchi method, the higher the η value, the better the overall performance, meaning that the factor levels with the highest η value should always be selected. Accordingly, the average for each experimental level was calculated using the highest η value for each factor to produce the response Table (Tables 4.5 and 4.6). As shown in the response Table, the optimum conditions to maintain the difference in the major strain$(\Delta\varepsilon)$ and the ductile fracture value I successfully in the forming test were $A_3B_3C_3$, which means R = 4 mm, H = 0.7 mm, and μ = 0.10 mm.

Figure 4.12 depicts the evolution of (FE) simulation results for the optimum conditions (A_3B_3-C_3) in incremental sheet forming process. Figure 4.13 shows the experimental result for optimum case, where no failure appeared in the concerned area.

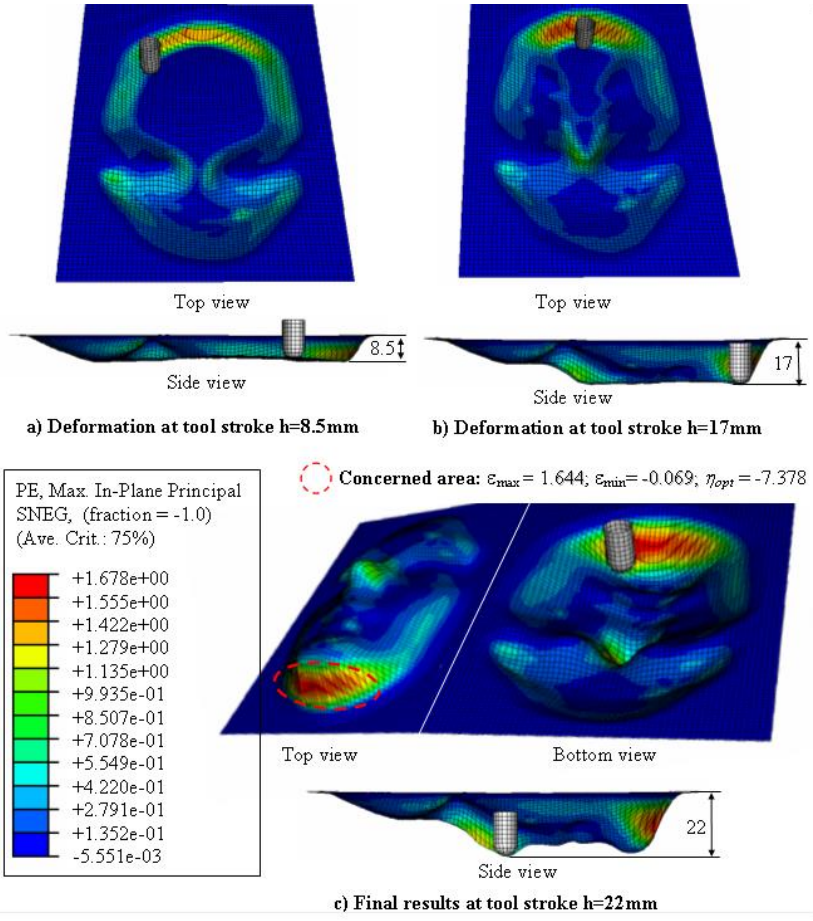

(i)

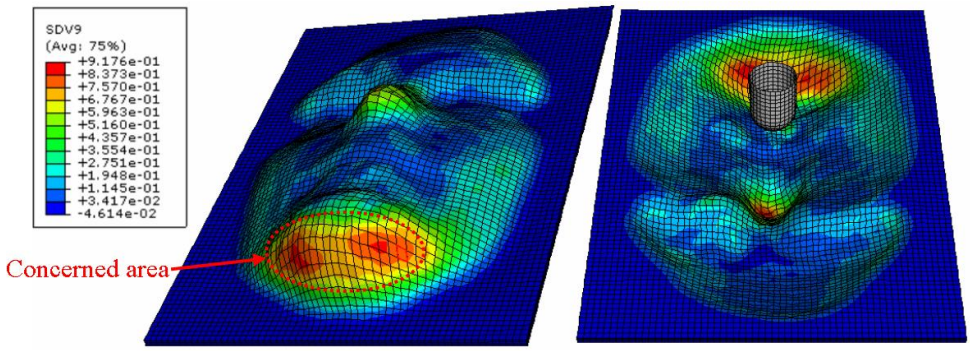

(ii)

Figure 4.12: *The evolution of deformed shape in FEM for optimum case of $A_3B_3C_3$ (i) and simulation result of I value (ii).*

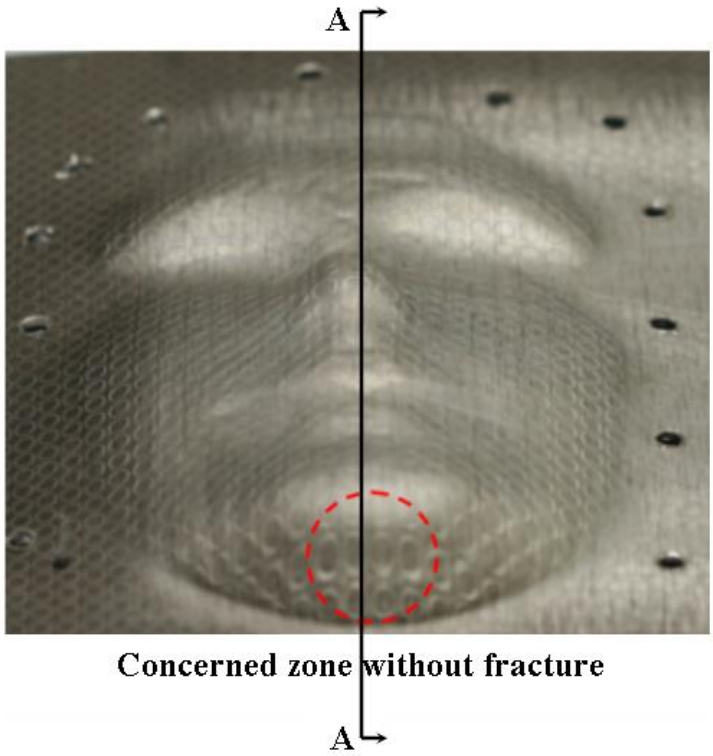

Figure 4.13: *Experimental result for optimum case of $A_3B_3C_3D_1$ (R=4mm, H=0.7mm, and $\mu=\mu_1=\mu_2=0.1$).*

Figure 4.14 presents the comparisons between cross-section views of evolutional stages of (FE) simulation and design section corresponding to side view in Figure 4.12 at each stage of tool stroke h = 8.5 mm, 17 mm, and 22 mm, respectively. Four different typologies of error can be detected on (FE) simulation results. First of all, a "pillow" effect can be highlighted at intermediate stages, determining a concave curvature of the under-formed material. Secondly, uncorrect tool paths generated at high slopes of sidewall, giving the big gap between final and design shape. Thirdly, due to a tool radius is larger than radii of curvature of design shape, although such inaccuracy is normally solved through using a smaller tool. Finally when the punch action is relaxed, the blank "lifts up" and the final depth of the part is lower than the design value.

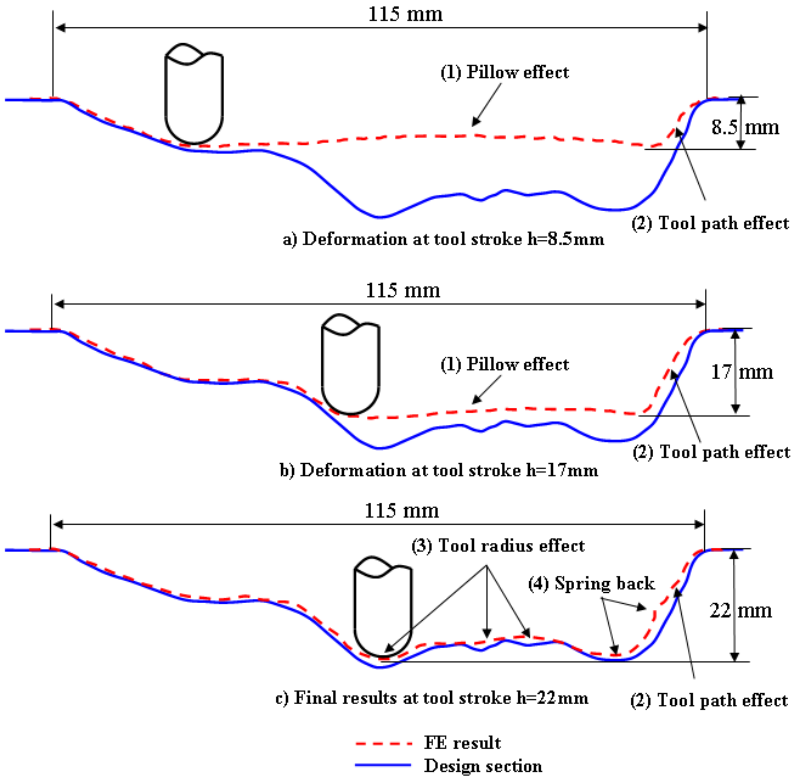

Figure 4.14: *Comparisons between section view of evolutional stages of FEM simulation and design section at tool stroke of h = 8.5mm, h = 17mm, and h = 22mm.*

To investigate and compare the accuracy of final shape between simulation and experiment, the cross-section AA in Figure 4.13 was measured to find out how much spring-back actually differed, see Figure 4.15. This figure shows that the difference of spring-back was larger at the surface profiles *cd* and *fg* due to the slopes of sidewall are larger than others surface profiles. The shape distribution of the surface profiles *ab*, *bc*, *de*, and *ef* has quite good agreement between the experimental and (FE) results.

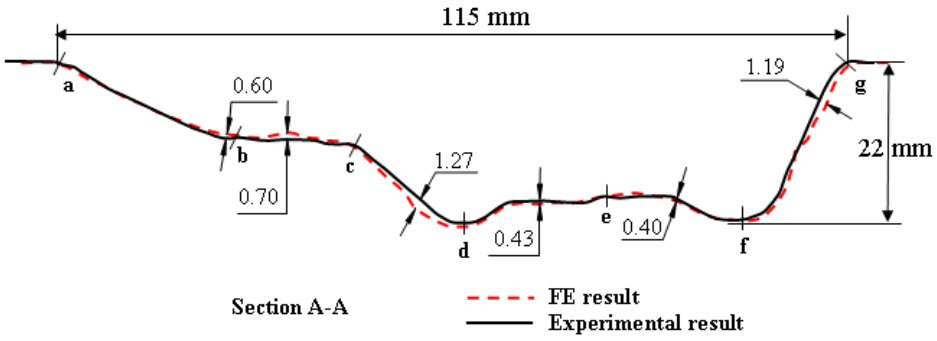

Figure 4.15: *Comparison of shape distribution between FE simulation and experiment results.*

From the above discussion, it was concluded that the use of Taguchi's experimental array for (FE) simulations allowed successful improvement of the process variables to improve the formability for incremental sheet forming process. As a result, the process variables were improved using a tool radius (R) of 4 mm, tool down step (H) of 0.7 mm, and friction coefficient (μ) of 0.1 mm.

4.7 Conclusion

To simulate the incremental sheet forming process of complex geometry shape e.g human face, values of (CL) data, which was generated from (CAM) simulation, has been automatically added and assigned to the (CAE) input file through MATLAB's subroutine programming.
To verify and improve process variables of incremental sheet forming process by using the finite element simulations, the tool radius, tool down step, and friction coefficient process variables was selected as main process variables and then investigated by the experiments. Commercial software (ABAQUS version 6.5, explicit formulation) was used for the simulation according to the orthogonal array of Taguchi's method. As a result of the (FE) simulations based on the Taguchi orthogonal array, the tool down step (H) was identified as the important factors for improving the formability of the incremental sheet forming process. An improved parameter, consisting of a tool radius (R) of 4 mm, a tool down step (H) of 0.7 mm, and friction coefficient (μ) of 0.1 mm, were chosen to give the best results for proposed geometry, using incremental forming.

Chapter 5: Case Study for Magnesium Alloy Sheets to Predict Ductile Fracture of Rotational Incremental Forming

5.1 Introduction

As the lightest structural alloys, magnesium alloys have many advantages compared with steel, cast iron and even aluminum alloys [85]. However, the structural use of magnesium alloys is seriously restricted by their limited ductility at room temperature (RT) due to their hexagonal close-packed (HCP) crystal structure [86, 87].

At present, the magnesium alloys used for automobile parts are mainly processed by die casting [88, 89] that allows parts with complex geometry to be manufactured. Yet, the mechanical properties of such die cast parts invariably lack the required endurance strength and ductility [90]. As an alternative, the required mechanical properties for magnesium alloys can be achieved using a forming process instead of a die casting process. Parts manufactured by forming can have a fine-grained structure without porosity and improved mechanical properties, such as endurance strength and ductility [91]. Thus, research on mass produced magnesium alloy sheets has increased.

To widen the application of the alloys, researches on sheet forming of magnesium alloys at elevated temperatures has been made in several papers [90, 92, 93, 94]. Won *et al.* [95] investigated the mechanical properties of magnesium alloys at elevated temperatures and discovered that the Lankford value(R) for an AZ31 magnesium sheet decreases as the temperature increases. It was revealed that an AZ31 magnesium sheet becomes isotropic and re-crystallizes above 200°C. Won *et al.* [95] and Choo *et al.* [96] studied the formability of magnesium alloy sheets at high temperatures and concluded that a temperature over 200°C was required to achieve the safe forming of magnesium alloy sheets. Park *et al.* [97] studied and showed the possibility of cup incremental forming of magnesium sheet at room temperature with rotational, where the tool rotates itself. Their study show that even though the incremental sheet forming has been found to improve the forming limit for aluminum and steel sheets compared with press forming [59, 77], there has been little investigation of incremental sheet forming for magnesium because it is difficult to form at room temperature. Therefore, they proposed rotational incremental sheet forming (RISF), which was proven to improve the formability of sheet materials compared with incremental sheet forming due to large amount of heat were generated in the contact area due to friction energy at the tool-specimen interface and plastic deformation energy by the shear deformation.

In this study, the rotational incremental forming of magnesium alloy sheet for various wall angle of square shape are simulated using ABAQUS/Explicit finite element code. As the ductile failure criterion, the Oyane's fracture criterion via VUMAT user material based on a combined kinematic/isotropic hardening law and Johnson-Cook model is used to predict fracture at elevated temperatures which was generated by rotational tool and friction energy at the tool-specimen interface. Firstly, a combined kinematic/isotropic hardening law is applied for uni-axial tension-compression test at room temperature to determine the scalar parameter β which make the best fit of stress-strain curves between (FE) simulation and experiment results of magnesium alloy sheet. Johnson-Cook model is then utilized to predict the stress-strain curves at elevated temperatures and compared with measured values. Finally, based on the relationship between heat generation at the tool-specimen interface and various wall angles, the Oyane's fracture criterion is used to predict fracture for rotational incremental forming of magnesium alloy sheets. The effect of process parameters on ductile fracture value and forming limit curve at fracture were also investigated.

5.2 Finite element procedures

In FEM simulation, due to asymmetric yield surface, the uniaxial-stress-plastic-strain response of the material for the uni-axial compression test is assumed as Equation (5.1):

$$\bar{\sigma}^C = \frac{\sigma_Y^C}{\sigma_Y^T} K(\varepsilon_0 + \varepsilon_{eq}^{pl})^n \tag{5.1}$$

Where K is the plastic coefficient,σ_Y^T,σ_Y^C are tension and compression yield stress, n is the work-hardening exponent, and $\bar{\sigma}^C, \bar{\varepsilon}_{eq}^{pl}, \varepsilon_0$are the equivalent stress in compression zone, equivalent strain, and yield strain, respectively, which were mentioned in Table 5.1.

Table 5.1: *Maximum temperature of the tool and specimen for each square cup (Ref. [97])*

Wall angle, θ (°)	Temperature of tool, (°C)	Temperature of specimen, (°C)
45	105	100
60	125	118
70	150	141

Figure 5.1 shows the stress-strain curves obtained from the in-plane uni-axial compression and tension tests at room temperature. Figure 5.2 shows experimental results for the yield loci, which were not symmetric, and the compressive behavior differed from the tensile behavior. These phenomena were unique behavior of magnesium alloy sheet because of its crystal structure.

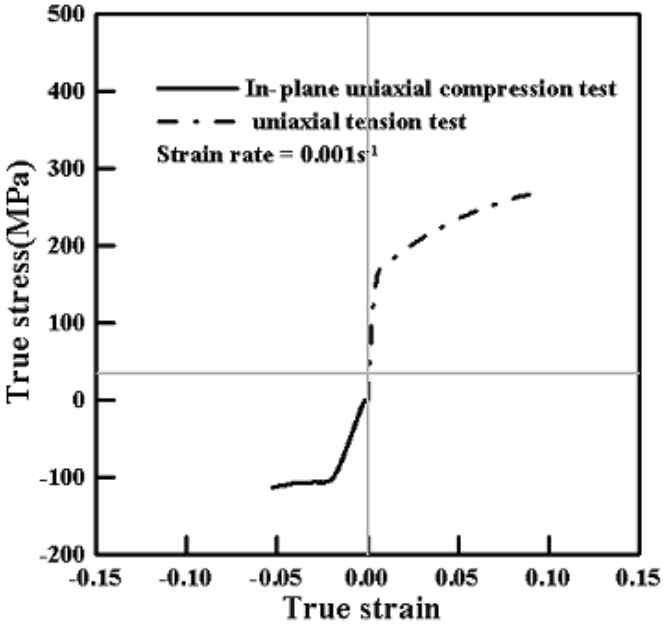

Figure 5.1: *Stress-strain curves obtained from in-plane uniaxial compression tests at room temperature (Ref. [97])*

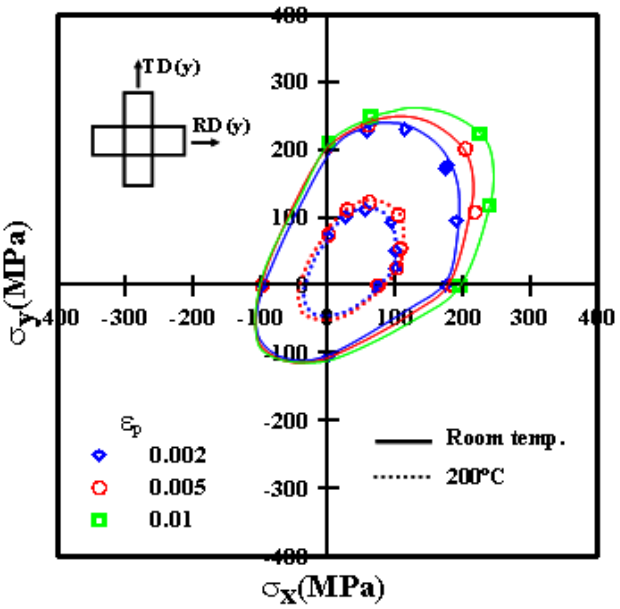

Figure 5.2: *Yield loci obtained from biaxial tensile tests and in-plane uniaxial compression tests (Ref. [97])*

In this chapter, due to low average R-value (Lankford value) at elevated temperature (R~1 at 200^0C), the Von-Mises model was assumably applied in calculation.

5.2.1 Johnson–Cook model at elevated temperatures

The inelastic behavior of the investigated alloy is assumed to be described by Johnson–Cook model [98]. This material model is suited to describe the mechanical behavior of material at high strain rates and various temperatures. It is generally used in adiabatic transient dynamic analysis. The hardening is a particular type of isotropic hardening in which the yield stress $\bar{\sigma}$ is assumed to be of the form:

$$\bar{\sigma} = (A + B(\varepsilon_{eq}^{pl})^n)\left(1 + C\, log\left(\frac{\dot{\varepsilon}_{eq}^{pl}}{\dot{\varepsilon}_0}\right)\right)(1 - \hat{T}^m) \tag{5.2}$$

where

$$\hat{T} = \begin{cases} 0 & for \quad T < T_r \\ \frac{T - T_r}{T_m - T_r} & for \quad T_r \le T \le T_m \\ 1 & for \quad T > T_m \end{cases} \tag{5.3}$$

A, B, C, n and *m* are material parameters, to be identified. T is the current temperature, T_m is the melting temperature and T_r is a reference temperature of 24 ◦ C.

In this study, we verify the unusual plastic behavior for magnesium sheet at elevated temperatures with constant strain rate ($\dot{\varepsilon}_0 = \dot{\varepsilon}_{eq}^{pl}$). Besides, the stress-strain curve has been fitted as in Equation 3.1. So that Equation (5.2) can be expressed as following reduced form

$$\bar{\sigma} = K(\varepsilon_0 + \varepsilon_{eq}^{pl})^n \left(1 - \left(\frac{T - T_r}{T_m - T_r}\right)^m\right) \tag{5.4}$$

To determine *m* quasi static experimental results at both room and higher temperatures are needed. If quasi static experiments, at the same strain rate, are carried out at two different temperatures denoted by the superscripts (5.2) and (5.3), the ratio *r* between the stresses at a specific plastic strain can be expressed as:

$$r = \frac{\bar{\sigma}^{(1)}(\varepsilon_{eq}^{pl})}{\bar{\sigma}^{(2)}(\varepsilon_{eq}^{pl})} = \frac{1 - (\hat{T}^{(1)})^m}{1 - (\hat{T}^{(2)})^m} \tag{5.5}$$

If $T^{(2)} = T_r$ then from Equation (5.2) $\hat{T}^{(2)} = 0$ and *m* is given by

$$m = \frac{log(1 - R)}{log(\hat{T}^{(1)})} \tag{5.6}$$

The stresses shown in Figure 5.3 for temperatures 100 ° C, 150 ° C and 200 ° C are divided by the stresses at 24 ° C (room temperature) according to Equation (5.5). The result is as well as the average values in the range $0.05 < \varepsilon^{pl} < 0.25$. The averaged values are r = 0.879, r = 0.712 and r = 0.444 for 100 ° C, 150 ° C and 200 ° C respectively. Substituting these values into Equation (5.6) results in m = 1.027 for 100 ° C, m = 0.802 for 150 ° C, and m = 0.48 for 200 ° C.

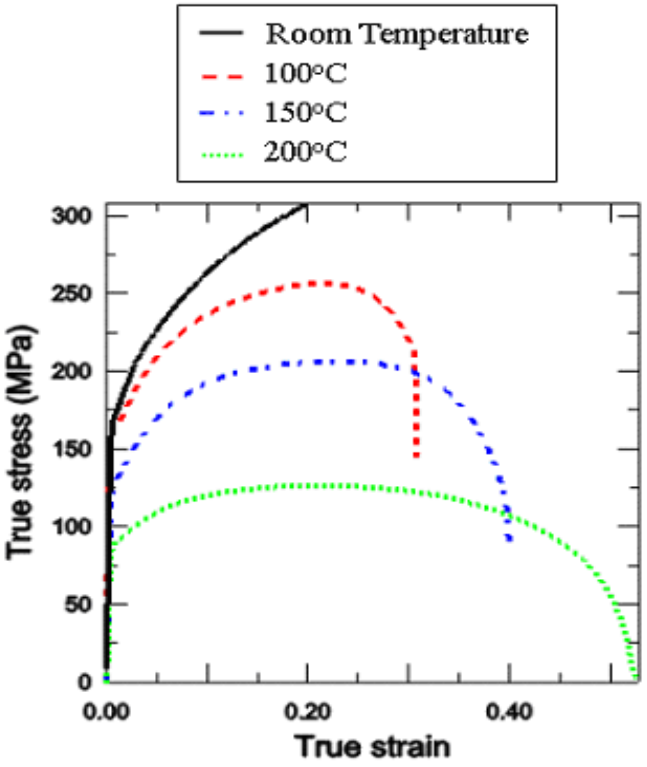

Figure 5.3 *The stress-strain curves with measured values [97]*

By adopting Johnson–Cook model thought using Equation (5.7) instead of Equation (3.1) in VUMAT subroutine for tensile test simulation at 100 ° C, 150 ° C and 200 ° C we can obtain the FE simulation results in Figure 5.4

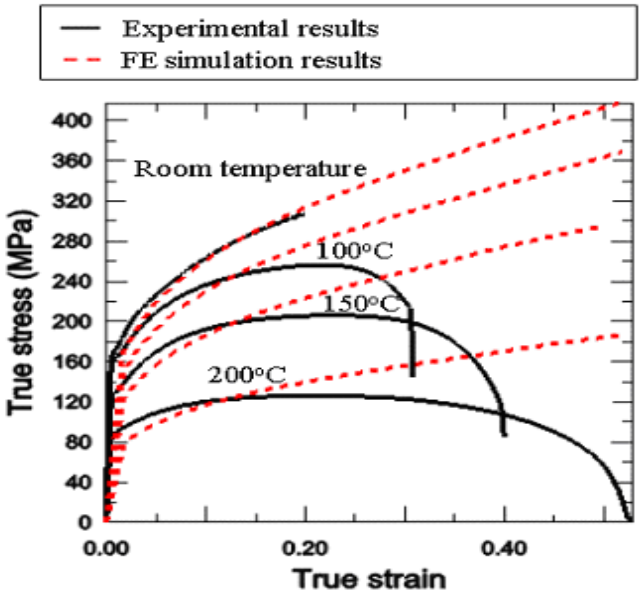

Figure 5.4: *The stress-strain curves calculated using FE simulation and compared with the measured values*

5.2.2 Problem description, geometry and FE models for rotational incremental forming of magnesium alloy sheet

In this study, we applied above model for square shape rotational incremental forming of magnesium alloy sheet. Here, the specimens were 150 mm (width) by 150 mm (length) by 1 mm (thickness). Meanwhile, the experimental model of the square shape was 80 mm (width) by 80 mm (length) by 25 mm (height). The depth increment was 0.4 mm in the z-direction, and the wall angles of the square cup shape were determined as 45 °, 60 °, and 70 °, respectively. The tool radius was 6mm and the feed rate was 400mm/min. As following previous study [97], in experiment the spindle speed of the tool was 4000 rpm on count clock wise for –z-direction until the temperature of the tool was 100 ° C in case of 45 ° wall angle and then set to 3000 rpm. Due to the temperature of the tool exceeded 100°C, chips of magnesium were generated in the contact area between the specimen and the tool. Therefore, 100 ° C is maximum temperature in case of 45 ° wall angle without chip generating. As same way, for the other case, maximum temperature was measured while Table 5.2 shows the maximum temperature of the tool and specimen for each square cup.

Table 5.2: *Thermo-physical properties of magnesium alloy AZ31 as function of temperature T (in ° C) [99]*

Thermo-physical property	AZ31
Thermal conductivity (W/(m K))	77 + 0.096 T
Specific heat capacity (J/(kg K))	1000 + 0.666T
Thermal coefficient expansion (K^{-1})	2.48e-05

As previous experiments [97], no fractures were observed with the 45 ° wall angle but fractures were observed with the 70° wall angle (Figure 5.5). The minor and major strains of a, b, c, d, and e in Figure 5.5 (c) were measured and represented as shown in Figure 5.6. Here, the open symbol of (△, □, ○) represents the strain with 45 °, 60 °, 70 ° wall angles and no fractures. Otherwise, the cross symbol (×) represents the occurrence of a fracture in wall and corner areas with a 70 ° wall angle.

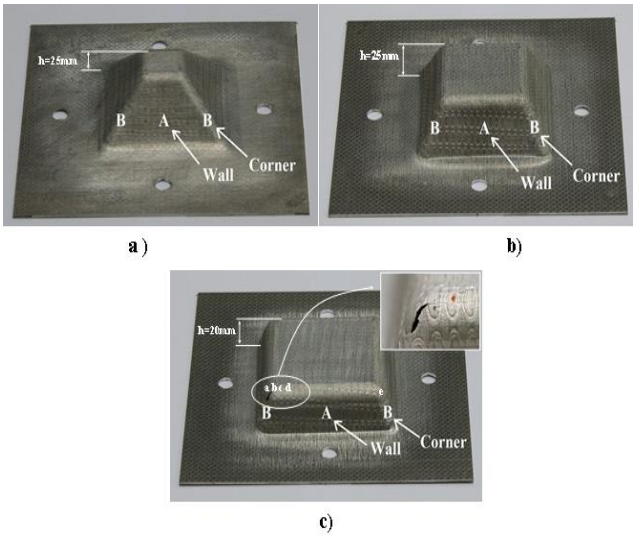

Figure 5.5: *The square cups formed by rotational incremental sheet forming of (a) 45° wall angle, (b) 60° wall angle, and (c) 70° wall angle at which the crack was occurred (Ref. [19]).*

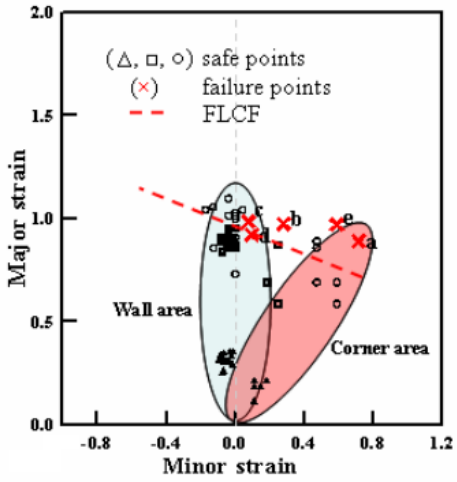

Figure 5.6: *Forming limit for rotational incremental forming*

As mention from the previous literature [59, 77], most forming limit curves in incremental sheet forming (FLC at fracture: FLCF) appears to be a straight line with a negative slope in the positive region of the minor strain. By adopting this linear model (Figure 5.6) to formulate a forming limit curve (FLCF), it can be expressed as follow:

$$\varepsilon_1 + 0.639\varepsilon_2 = 1.02 \quad (5.7)$$

Figure 5.7 shows the finite-element model for the incremental sheet forming test process. To simulate the experiments, only one quarter of specimen is modeled, the blank modeled using solid elements C3D8R, the punch modeled using analytical rigid surface-elements, and the die modeled using rigid surface-elements R3D4. Throughout this study, the average element size of the blank was about 1 mm in width, 1mm in length, and 0.33 in thickness; the average element size of the rigid die was about 2 mm in width, and 2 mm in length. Here, the die was fixed in all directions. The tool was allowed to move following the tool-path and rotate involving z direction at the centre point of the tool. The friction behavior was modeled using the Coulomb friction law. The friction coefficient μ_1 between the blank and the punch is assumed to be the same the fiction coefficient μ_2 between the blank and the die of 0.1. The other physical properties of the materials used in the analysis are shown in Table 5.2.

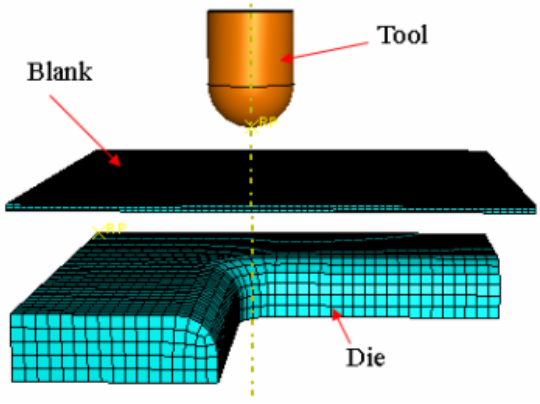

Figure 5.7: *Finite element model for incremental forming simulation*

5.2.3 Ductile fracture criterion

To determine the material constants C_1, C_2 in Equation (3.3), destructive tests have to be operated under at least two types of stress conditions. Here, we utilized forming limit curve at fracture Equation (5.7) to calculate the fracture strain for uni-axial tension and a plane strain state as 1.499 and 1.178, respectively. From this result, the material constants C_1, and C_2 for the ductile fracture criterion were calculated as 2.059, and 3.586, respectively.

Oyane's the ductile criterion in Equation (5.8) is combined with proposed hardening model and Johnson-Cook model, and then coded into a VUMAT subroutine.

5.3 Results and discussion

Figure 5.8 (a) shows the FE simulation results of heat generation (SDV44) in the contact area between the specimen and the tool for three different positions of tool, Figure 5.8 (b) depicts the evolutions of temperature at the elements corresponding to three tool positions of Figure 5.8 (a) for the case of 70 ◦ wall angle.

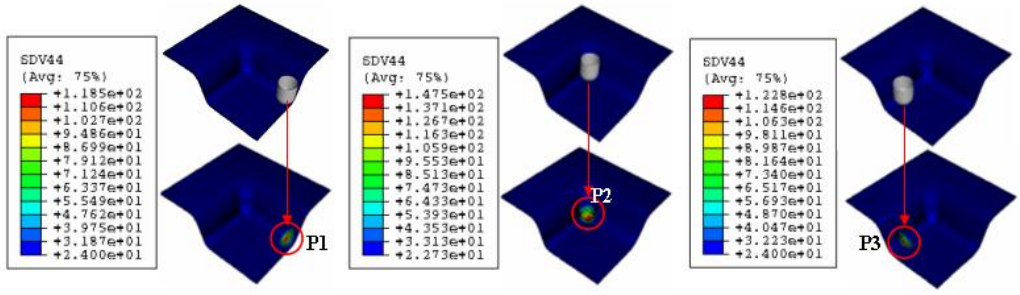

(a)

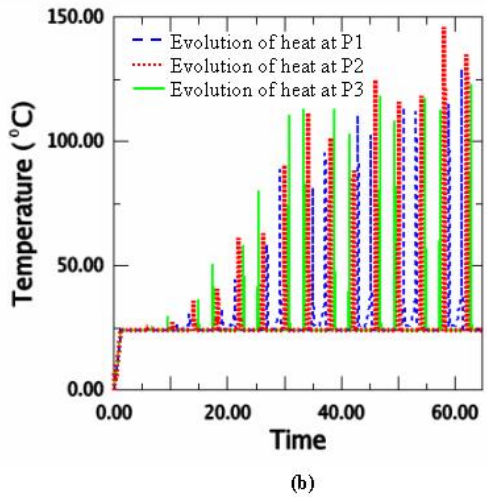

(b)

Figure 5.8: *Heat generation in the contact areas between the specimen and the tool*

The results show that the maximum temperatures in FE simulation of 147 ◦ C at corner and about 122 ◦ C at wall areas are good agreement with that in experimental measurement of 141 ◦ C given in Table 5.1. In order to verify the effect of heat generation on the stress-strain curve without considering Johnson-Cook model, equivalent stress-strain evolution in incremental forming, obtained by (FE) simulation via VUMAT user material, were compared with other stress-strain curves at elevated temperatures obtained by adopting Johnson–Cook model for tensile test simulation in Figure 5.4 and shown in Figure 5.9 (a).

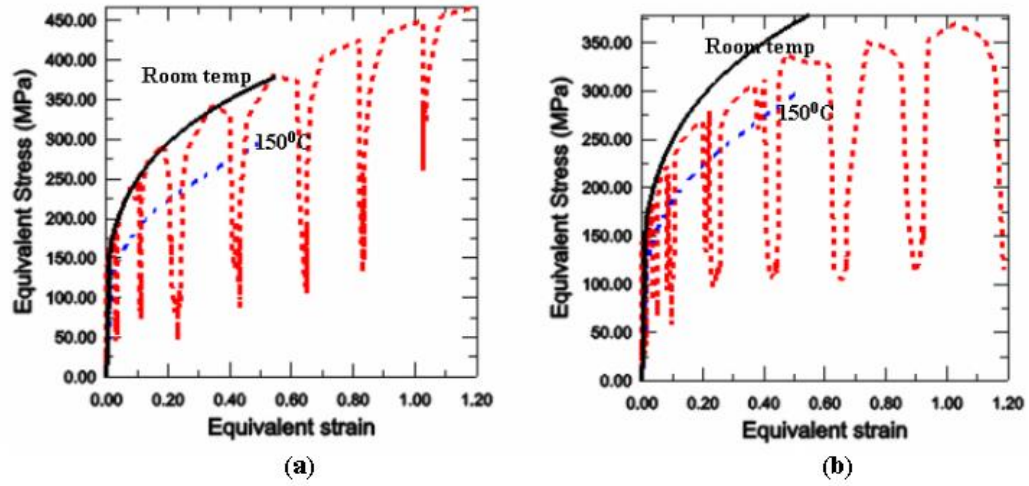

Figure 5.9: *Evolution of equivalent stress-strain curve in incremental forming in case of (a) without considering Johnson-Cook model and (b) considering Johnson-Cook model*

Even though the (FE) simulation predicts well heat generation, the boundary profile of equivalent stress-strain evolution in incremental forming without considering Johnson-Cook model was still following stress-strain curve at room temperature. So that, in this study, heat generation at elements in the contact area between the specimen and the tool was calculated considering Johnson-Cook model using Equation (5.4) and coded into VUMAT subroutine for incremental forming simulation. The equivalent stress-strain evolution in this case was shown in Figure 5.9(b). The boundary profile of equivalent stress-strain evolution, which was limited by stress-strain curves at room temperature and 150 ° C in tensile test simulation, proved the effect of heat generation on stress-strain curve and was suitable with experiments of tensile test at elevated temperatures. This method should be applied to predict ductile fracture in (FE) simulation of rotational incremental forming of magnesium alloy.

The (FE) simulation results for three cases test sample with the equivalent plastic strain $\bar{\varepsilon}$ (SDV7), and the maximum ductile fracture value *I* (SDV9) calculated from Equation (25) via VUMAT user material based on a combined kinematic/isotropic hardening law are presented in Figure 5.10. The simulation results show that the maximum value of the fracture ductile integral *I* of the (80 mm × 80 mm × 25 mm) square shape with 40^{o}, and 60^{o} wall angles

corresponding 105 ◦ C, and 126 ◦ C of maximum temperature are 0.513 and 0.898, respectively, which is smaller than 1.00. This means that failure do not occur in this case of process. Otherwise, in case of the (80 mm × 80 mm × 20 mm) square shape with 70 ◦ wall angle corresponding 147 ◦ C of maximum temperature, the (FE) simulation results give the maximum value of ductile fracture integral *I* equal to 1.242, and failure appeared. The trends of the failure site predicted in his study were in quite good agreement with those in the actual experiments.

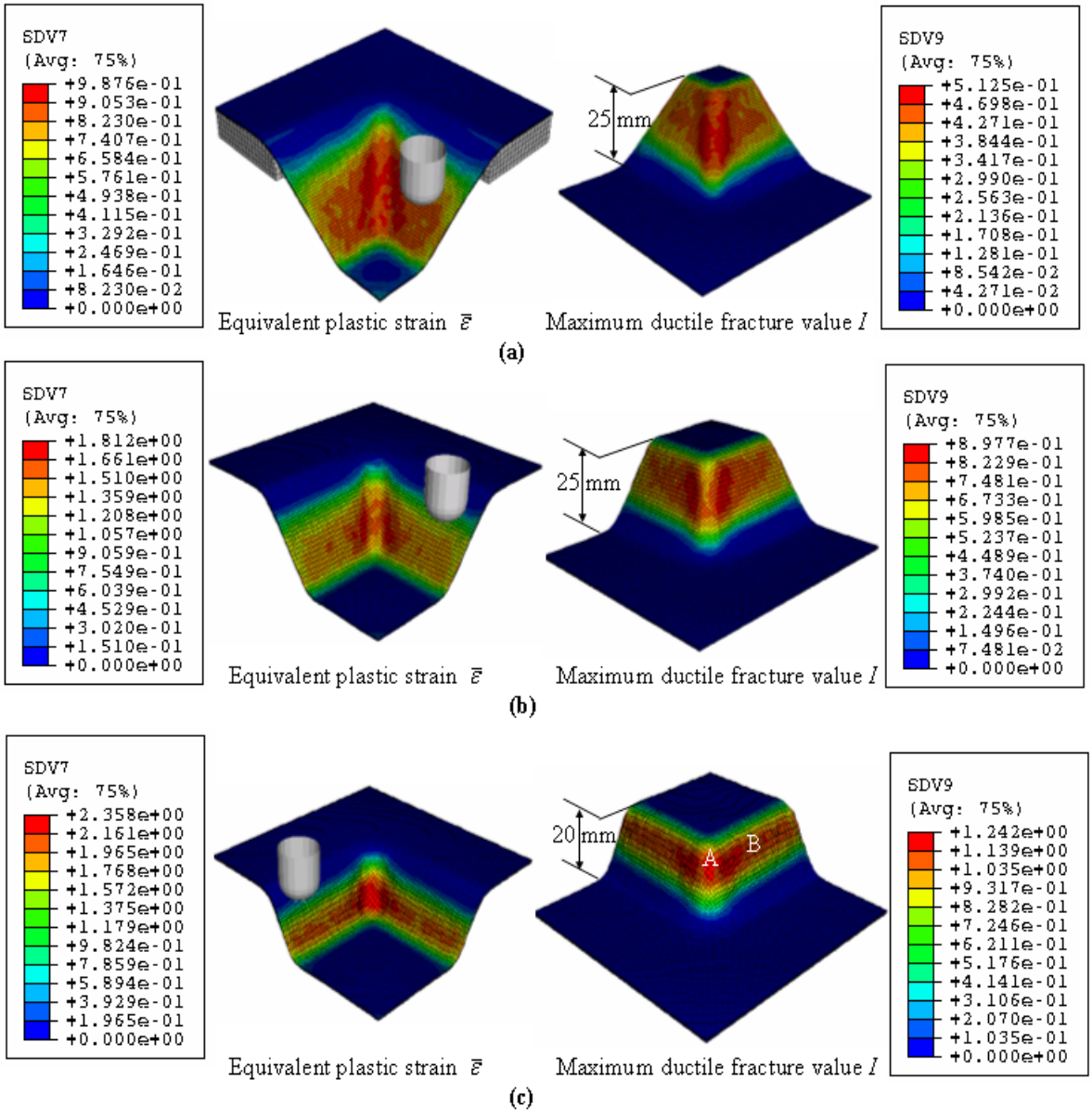

Figure 5.10: *Deformed shape in finite element simulation in case of (a) 45º wall angle, (b) 60º wall angle, and (c) 70º wall angle*

After the simulation, it can be concluded that in order to obtain a sound final product, the wall angle of the square shape should be smaller than 70 °. Even though the heat generation is smaller than the case of 70 ° wall angle, 45 ° and 60 ° wall angles can be deformed to the final shape without any failure.

In order to predict forming limit curve at fracture utilized (FE) simulation results, we proposed the method as shown in Figure 5.11. Figure 5.11 (a) shows the evolutional strain paths at the element of corner area (point A in Fig 5.10 (c)) and the element of wall area (point B in Figure 5.10 (c)). These strain paths is suitable to the paths of equal biaxial stretching and plane strain. Figure 5.11 (b) presents the evolutions of the ductile fracture integral I at the elements of concerned points (A and B) versus major strain. From Figure 5.11 (b), the major strains at occurred fracture (I = 1) of concerned points of equal biaxial stretching and plane strain are determined as 0.665 and 1.017, respectively. Figure 5.11 (c) depicts the forming limit curve at fracture (FLCF) obtained by adopting a linear model through occurred fracture points from (FE) simulations. This (FLCF) is quite good agreement with the previous assumption of Equation (5.7) and Figure 5.6.

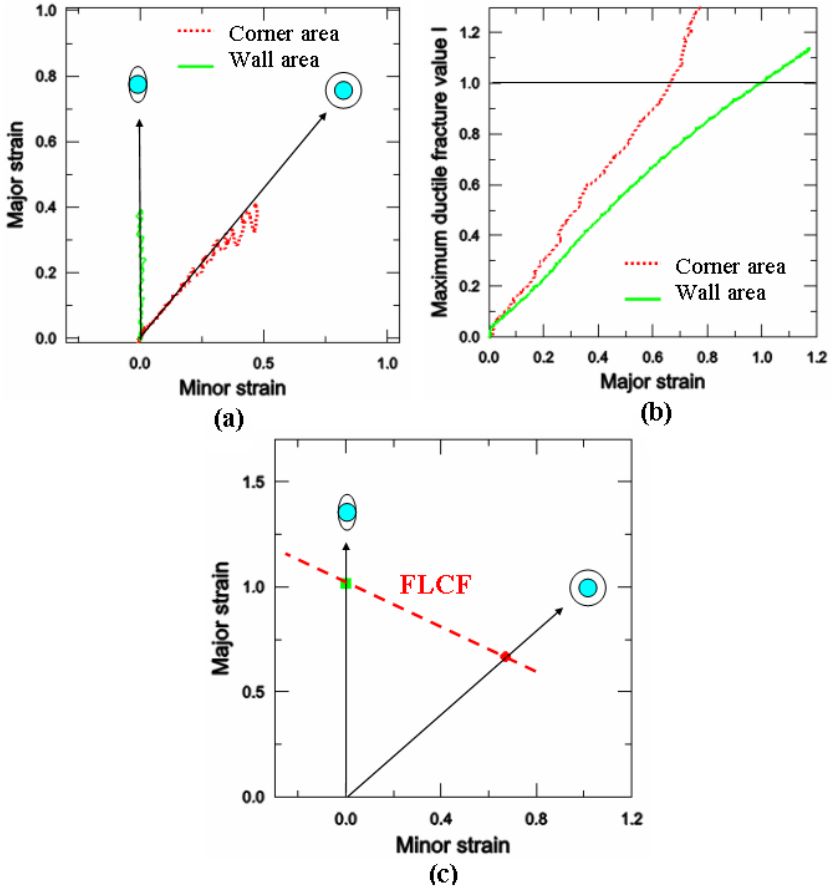

Figure 5.11: *FLCF obtainment from FE simulation at the corner and wall area for the case of 70^0 wall angle.*

5.3.1 Effect of tool down-step

To verify the effect of tool down-step (H), analysis is carried out for the tool down-step (H) of 0.8 mm, and 1.2 mm and then results are compared with that of H = 0.4 mm discussed earlier for the case of the (80 mm × 80 mm × 20 mm) square shape with 70° wall angle corresponded 140 ° C of temperature and the tool radius (R) of 6 mm. As shown in Figure 5.12, the maximum values of ductile fracture integral *I* in these cases are predicted to be 1.271 and 1.324, respectively. Thus, at higher tool down-step, the maximum values of ductile fracture integral *I* will be larger. This happens, because deformation becomes larger with increase in tool down-step.

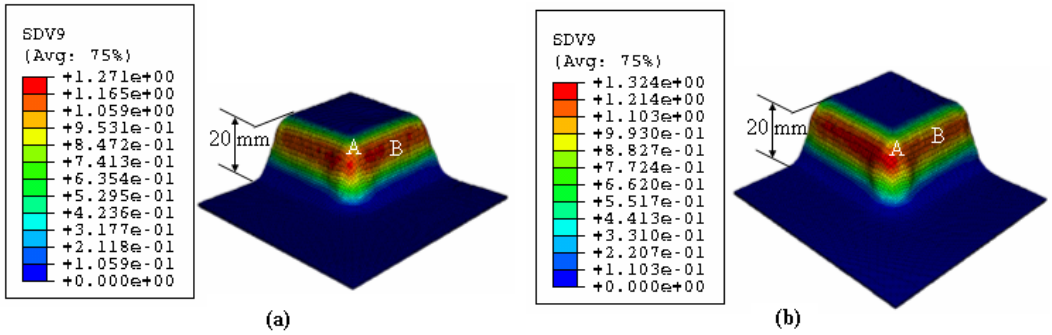

Figure 5.12: *Deformed shape in FE simulation in case of 70° wall angle, tool radius of 6 mm, and (a) tool down-step of 0.8 mm; (b) tool down-step of 1.2 mm*

Figure 5.13 presents the (FLCF) obtained by adopting a linear model through occurred fracture points (*I* = 1) of equal biaxial stretching and plane strain for all three cases. When the down-step increased from 0.4 mm to 0.8 mm, and 1.2 mm, the fracture major strains of equal biaxial stretching and plane strain decreased to 0.613, 0.544 and 0.94, 0.85, respectively, so that the (FLCF) moved down. Thus, it is clear that the formability becomes lower as the down-step becomes higher. These results were similar to the experimental results and conclusions of previous study [77].

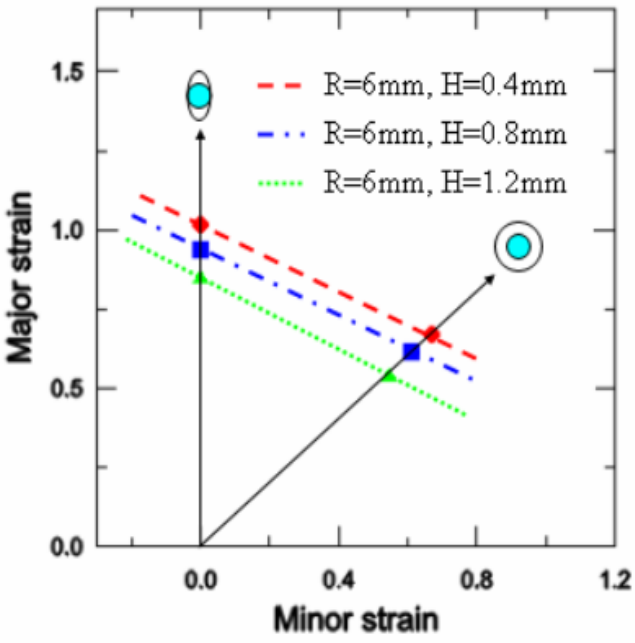

Figure 5.13: *FLCF with different tool down-step and 6 mm tool radius*

5.3.2 Effect of tool radius

The effect of tool radius (R) is investigated by carrying out the analysis for the following two cases of R = 4 mm, and 8 mm. The analysis is carried out for the case of the (80 mm × 80 mm × 20 mm) square shape with 70 ° wall angle and the tool down-step (H) of 0.4 mm. The maximum values of ductile fracture integral *I* was found to be 1.229, and 1.258, respectively as shown in Figure 5.14. Figure 5.15 depicts the (FLCF) when the tool radius changes from 6 mm to 4 mm and 8 mm. The (FLCF) is lower in case of 8mm tool radius with the fracture major strains of equal biaxial stretching and plane strain is 0.614, and 0.927, respectively. In the case of 4 mm tool radius, the fracture major strain increased to 0.717 at equal biaxial stretching and decreased to 0.597 at plane strain area. As the tool radius increases, the deformation zone or the contact zone increases, and the level of strain decreases resulted incremental formability.

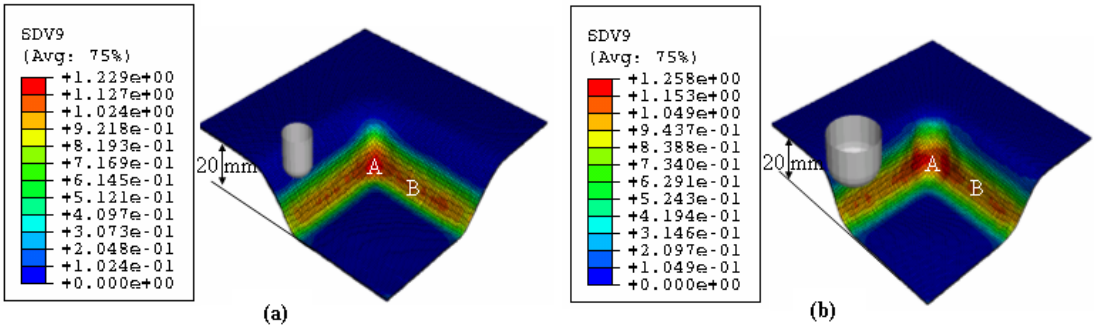

Figure 5.14: *Deformed shape in FE simulation in case of 70 ° wall angle, tool down-step of 0.8 mm, and (a) tool radius of 4 mm; (b) tool radius of 8 mm*

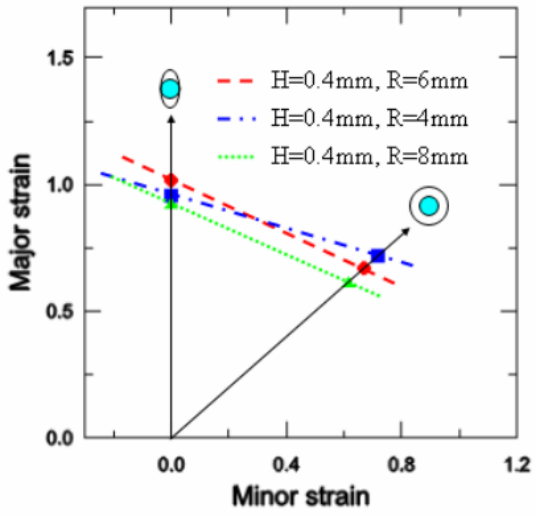

Figure 5.15: *FLCF with different tool radius and 0.4 mm tool down-step*

5.4 Conclusion

In this study, to predict a fracture of rotational incremental forming for magnesium alloy sheet, the heat generation at elements due to rotational tool and contact area between the specimen and the tool was implemented using finite element simulations through Johnson-Cook model and then compared with experiments of the square shape with 45 °, 60 °, and 70 ° wall angles. Commercial software (ABAQUS version 6.5, explicit formulation) with a user-defined subroutine (VUMAT) based on a combined kinematic/isotropic hardening model was used for the simulation. The (FE) simulation results show that if the wall angles of 80 mm × 80 mm × 25mm square shape are smaller than 60 ° then the maximum value of the fracture ductile integral *I* will be less than 1 value, and fracture will not occur. The predictions of failure site were in good agreement with those in actual experiments. The (FLCF) prediction and effect of process parameters on (FLCF) utilized (FE) simulation results show that the formability decreases as the tool down-step or tool radius increase. This prediction is suitable to previous conclusion [77] of incremental sheet forming process.

Bibliography

[1] R.K. Boger, R.H. Wagoner, F. Barlat, M.G. Lee and K. Chung, Continuous, large strain, tension/compression testing of sheet material, *Int. J. Plast.* **21** (2005) (12), pp. 2319–2343.

[2] W. Prager, A new method of analyzing stresses and strains in work hardening. Plastic Solids, *J. Appl. Mech. ASME* **23** (1956), p. 493.

[3] H. Ziegler, A modification of Prager's hardening rule, *Quart. Appl. Math.* **17** (1959), p. 55.

[4] Amstrong, P.J., Frederick, C.O., 1966. A Mathematical Representation of the Multiaxial Bauschinger Effect. G.E.G.B. Report RD/B/N 731.

[5] J.L. Chaboche, Time independent constitutive theories for cyclic plasticity, *Int. J. Plasticity* **2** (1991), p. 149.

[6] N. Ohno and J.D. Wang, Nonlinear hardening rules with critical state of dynamic recovery. Part I: formulation and basic features for ratcheting behavior, *Int. J. Plasticity* **9** (1993), p. 375.

[7] N. Ohno and J.D. Wang, Nonlinear hardening rules with critical state of dynamic recovery. Part II: application to experiments of ratcheting behavior, *Int. J. Plasticity* **9** (1993), p. 391.

[8] N. Ohno and Y. Kachi, A constitutive model of cyclic plasticity for nonlinear hardening materials, *J. Appl. Mech.* **53** (1986), p. 395.

[9] R.K. Boger, R.H. Wagoner, F. Barlat, M.-G. Lee and K. Chung, Continuous, large strain, tension/compression testing of sheet material, *Int. J. Plasticity* **21** (2005), p. 2319.

[10] R.D. Krieg, A practical two surface plasticity theory, *J. Appl. Mech. ASME* **42** (1975), p. 641.

[11] Y.F. Dafalias and E.P. Popov, Plastic internal variables formalism of cyclic plasticity, *J. Appl. Mech. ASME* **98** (1976), p. 645.

[12] Z. Mroz, On the description of anisotropic work-hardening, *J. Mech. Phys. Mech.* **15** (1967), p. 163.

[13] A.S. Khan and S. Huang, Continuum Theory of Plasticity, John Wiley & Sons, Inc., NY, USA (1995).

[14] Z. Mroz, V.A. Norris and O.C. Zienkiewicz, Application of an anisotropic hardening model in the analysis of deformation of solids, *Geotechnique* **29** (1979), p. 1.

[15] K. Hashiguchi, Constitutive Equations of elastoplastic materials with anisotropic hardening and elastic–plastic transition, *J. Appl. Mech. ASME* **48** (1981), p. 297.

[16] D.L. McDowell, A two surface model for transient nonproportional cyclic plasticity: Part 1: development of appropriate Equations, *J. Appl. Mech. ASME* **52** (1985), p. 298.

[17] K. Hashiguchi, A mathematical modification of two surface model formulation in plasticity, *Int. J. Solids Structures* **24** (1988), p. 987.

[18] A.R. Khoei and N. Jamali, On the implementation of a multi-surface kinematic hardening plasticity and its applications, *Int. J. Plasticity* **21** (2005), p. 1741.

[19] M.G. Lee, D. Kim, C. Kim, M.L. Wenner, R.H. Wagoner and K. Chung, A practical two-surface plasticity model and its application to springback prediction, *Int. J. Plasticity* **23** (2007), pp. 1189–1212.

[20] Z. Mroz, An attempt to describe the behavior of metals under cyclic loads using a more general work hardening model. *Acta Mechanica*, 7: 199–212, 1969.

[21] P.G. Hodge, A new method of analyzing stresses and strains in work hardening plastic solids. *Journal of Applied Mechanics*, 24: 482–483, 1957.

[22] J.F. Besseling, A theory of elastic, plastic, and creep deformation of an initially isotropic material showing strain hardening, creep recovery, and secondary creep. *Journal of Applied Mechanics*, 25: 529-536, 1958.

[23] D.W.A. Rees, Anisotropic hardening theory and the Bauschinger effect. *Journal of Strain Analysis*, 16: 85-95, 1981.

[24] W. Prager, The theory of plasticity: A survey of recent achievements. *Proceedings of the Institution of Mechanical Engineers*, 169: 41, 1955.

[25] W. Prager, Recent developments in the mathematical theory of plasticity. *Journal of Applied Physics*, 20: 235-241, 1949.

[26] C. Teodosiu and Z. Hu. Evolution of the intragranular microstructure at moderate and large strains: modelling and computational significance. in *Proceedings of Numiform'95 on Simulation of Materials Processing: Theory, Methods and Applications*. Balkema, Rotterdam. 173–182, 1995.

[27] S. Li, E. Hoferlin, A. Van Bael, et al., Finite element modeling of plastic anisotropy induced by texture and strain-path change. *International Journal of Plasticity*, 19: 647-674, 2003.

[28] C. Teodosiu and Z. Hu. Microstructure in the continuum modelling of plastic anisotropy. in *Proceedings of the 19th Riso International Symposium on Materials Science: Modelling of Structure and Mechanics of Materials from Microscale to Product*. Riso National Laboratory, Roskilde, Denmark. 149-168, 1998.

[29] Z. Hu, Work-hardening behavior of mild steel under cyclic deformation at finite strains. *Acta Metallurgica et Materialia*, 42: 3481-3491, 1994.

[30] Z. Hu, E.F. Rauch, and C. Teodosiu, Work-hardening behavior of mild steel under stress reversal at large strains. *International Journal of Plasticity*, 8: 839-856, 1992.

[31] E. Hoferlin, A. Van Bael, P. Van Houtte, et al. An accurate model of texture and strain-path induced anisotropy. in *Proc. of the 4th Int. Conf. and Workshop on Numerical Simulation of 3D.*

[32] Hibbitt, Karlsson, and Sorenson, ABAQUS Theory Manual, Pawtucket, RI, USA, 1997.

[33] Simo, J. C., Kennedy, J. G. and Govindje, S., Non-smooth multisurface plasticity and viscoplasticity. Loading/unloading conditions and numerical algorithms, international journal for numerical methods in engineering, 1988; 26:2161-2185

[34] Simo, J. C., Algorithms for static and dynamic multiplicative plasticity that preserve the classical return mapping schemes of the infinitesimal theory, Computer Methods in Applied Mechanics and Engineering, 1992; 99:62-112

[35] Zavaliangos, A. and Anand, L., Thermal aspects of shear localization in microporous viscoplastic solids, international journal for numerical methods in engineering, 1992; 33:595-634.

[36] Guo, Y.Q., Li, Y.M., Bogard, F., and Debrey, K. An efficient pseudo-inverse approach for damage modelling in the sheet metal forming process. *J. Mater. Process. Technol*, 2004, **151**, 88–97.

[37] Wang, C.T., Kinzel, G., and Altan, T. Failure and wrinkling criteria and mathematical modeling of shrink and stretch flanging operation in sheet-metal forming. *J. Mater. Process. Techno*, 1995, 53, 759–780.

[38] Takuda, T., Mori, K., Fujimoto, H., and Hatta, N. Prediction of forming limit in bore-expanding of sheet metals using ductile fracture criterion. *J. Mater. Process. Technol*, 1999, 92–93, 433–438.

[39] Clift, S.E., Hartley,P., Sturgess, C.E.N., and Rowe, G.W. Fracture prediction in plastic deformation process. *Int. J. Mech. Sci*, 1990, 32, 1–17.

[40] Kim, Y.S. and Park, K.C. Sensitivity Analysis of Material and Process Variables Affecting on the Stamping Formability. *J. Kor. Soc. Mech. Eng. A*, 1996, 20, 2246-2256.

[41] Elsayed, E.A. and Hsiang, T. *Quality Engineering in Production Systems*. McGraw-Hill, New York, 1989.

[42] Bendell, A., Disney, J., and Pridmore, W.A. *Taguchi Methods-Application in World Application*. Industries, Productivity, Improvement and Case Study, IFS Publication, UK, 1989.

[43] Taguchi, G. *On-line Quality Control during Production*. Japan Standard Association, Tokyo, 1981.

[44] Nguyen, D.T., Choi, S.G, Park, J.Y., Suh, Y.S., and Kim, Y.S. Finite Element Method simulations to improve press formability of door hinge. *J. Mater. Eng. Performance*, 2009, in press.

[45] Wang, G.G. and Shan. S. Review of Metamodeling Techniques in Support of Engineering Design Optimization. *J. Mech. Design*, 2007, 129(4), 370-380.

[46] Delameziere, A., Naceur, H., Breitkopf, P., Knopf-Lenoir, C., Batoz, J.L. and Villon, P. Feasibility in deep drawing: optimization of material properties using response surface. *Mech Ind*, 2002, **3** (2), 93–98.

[47] Wang, H., Li, G.Y. and Zhong, Z.H. Optimization of sheet metal forming processes by adaptive response surface based on intelligent sampling method, *J Mater Process Tech*, 2008, **197** (1–3), 77–88.

[48] Zhang, X., Cheng, G., Wang, B. and Zhang, H. Optimum design for energy absorption of bitubal hexagonal columns with honeycomb core, *Int J Crashworthiness*, 2008; 13(1), 99-107.

[49] Untaroiu, C.D., Shin, J. and Crandall, J.R. A design optimization approach of vehicle hood for pedestrian protection, *Int J Crashworthiness*, 2007; 12(6), 581-589.

[50] Oyane, M., Sato, T., Okimoto, K., and Shima, S. Criteria for ductile fracture and their applications. *J. Mech. Work. Technol*, 1980, 4, 65–81.

[51] Swift, H.W., Plastic instability under plane stress, *J. Mech. Phys. Solids.*, 1952, **1**, 1–18.

[52] Toda, M., Miki, T., Yanagimoto, S., and Osakada, K. Study of computer aided system for analyzing mechanical behavior of steel bar and wire under cold forging. *J. Jpn. Soc. Tech. Plasticity*, 1988, 29, 971–976.

[53] Takuda, H., Mori, K., Fujimoto, H., and Hatta, N. Prediction of forming limit in deep drawing of Fe/Al laminated composite sheets using ductile fracture criterion. *J. Mater. Process. Technol*, 1996, 60, 291–296.

[54] Ko, Y.K., Lee, J.S., Huh, H., Kim, H.K., and Park, S.H. Prediction of fracture in hub-hole expanding process using a new ductile fracture criterion. *J. Mater. Process. Technol*, 2007, **187-188**, 358–362.

[55] Avitzur, B. and Yang, CT. Analysis of power spinning of cones, *J. Eng.Ind., Trans. ASME,*1960, 82, 231-45.

[56] Kalpakcioglu, S. A study of shear-spinnability of metals. *J. Eng.Ind., Trans. ASME*, 1961, 83, 485-95.

[57] Powell, NN. and Andrew, C. Incremental forming of angled sheet metal components without dedicated dies. *Proc. Inst. Mech., Eng, 1992, 206, 41-47.*

[58] Matsubara, S. Incremental backward bulge forming of a sheet metal with a hemispherical head tool. *J. Japan Soc. Technol. Plasticity.*, 1994, 35(406), 1311-1316.

[59] Iseki, H. and Kumon, H. Forming limit of incremental sheet metal stretch forming using spherical rollers. *J. Japan Soc. Technol. Plasticity.*, 1994, 35(406), 1336-1341.

[60] Fratini, L., G., Ambrogio, G., Di Lorenzo, R., L., Filice, L., and Micari, F. Influence of mechanical properties of the sheet material on formability in single point incremental forming, *Ann. CIRP*., 2004, **53**(1), 207–210.

[61] Kim, Y.H. and Park, J.J. Effect of process parameters on formability in incremental forming of sheet metal, *J. Mater. Process. Technol.*, 2003, 130/131, 42–46.

[62] Ambrogio, G., Costantino, I., De Napoli, L., Filice, L., Fratini, L. and Muzzupappa, M. Influence of some relevant process parameters on the dimensional accuracy in incremental forming: a numerical and experimental investigation, *J. Mater. Process. Technol.*, 2004, 153C/154C, 501–507.

[63] Kim, T.J. and Yang, D.Y. Improvement of formability for the incremental sheet metal forming process. *Int. J. Mech. Sci.*, **2000, 42**, 1271-1286.

[64] Hussain, G. and Gao, L.A novel method to test the thinning limits of sheet-metals in negative incremental forming, *Int. J. Mach. Tools. Manuf.*, 2007, **47**, 419–435.

[65] Hussain, G., Gao, L., and Dar, N.U. An experimental study on some formability evaluation methods in negative incremental forming, *J. Mater. Process. Technol.*, 2007, **18**, 45–53.

[66] Hussain, G., Gao, L., Hayat, N., and Qijian, L. The effect of variation in the curvature of part on the formability in incremental forming: An experimental investigation, *Int. J. Mach. Tools. Manuf.*, 2007, 47, 2177-2181.

[67] Park, J.G., You, B.S., and Kim, Y.S. A parametric study in incremental forming of magnesium alloy sheet, *Trans. Mate, Process.*, 2008, 17, 412-419.

[68] Ambrogio, G., Cozza, V., Filice, L., and Micari, F. An analytical model for improving precision in single point incremental forming, *J. Mater. Process. Technol.*, 2001, 191(1/3), 92-95.

[69] Lee, C.H. and Kobayashi, S. New Solutions to Rigid Plastic Deformation Problems Using Matrix Methods, *Trans. ASME, J. Eng. Ind.*, 1973, 95, 865-873.

[70] Lung, M. and Mahrenholtz, 0. A finite element procedure for analysis of metal forming processes. *Trans. CSME.*, 1973-1974, 2, 31.

[71] K. Mori, K., Osakada, K., and Oda, T. Simulation of plane-strain rolling by the rigid-plastic finite element method. *Int. J. Mech. Sci.*,1982, 24, 519.

[72] Tomita, Y. Simulation of plastic instabilities in solid mechanics, *Applied Mechanics Review.*, 1994, 47 (6), 171.

[73] Richelsen, A.B. Elastic–plastic analysis of the stress and strain distributions in asymmetric rolling, *Int. J. Mech. Sci.*, 1997, **39**, 1199.

[74] Wang, N.M. and Budiansky, B. Analysis of sheet metal stamping by a finite element method, *ASME J. Appl. Mechs.*, 1978, 45, 73-82.

[75] Ni, C.M. Stamping and hydroforming process simulation with a 3D finite element code. *SAE Technical Paper.*, 1994, 940753, 512-534.

[76] Comsa, D.S., Cosovici, G., Jurco, P., Paraianu, L., and Banabic, D. Simulation of the hydroforming process using a new orthotropic yield criterion. *J. Mater. Proces. Technol.*, 2004, 157-158, 67-74.

[77] Sim, M.S. and Park, J.J. The formability of aluminum sheet in incremental forming, *J. Mater. Process. Technol.*, 2001, 113, 654-658.

[78] Iseki, H. An approximate deformation analysis and FEM analysis for the incremental bulging of sheet metal using a spherical roller, *J. Mater. Proces. Technol.*, 2001, 111(1/3), 150-154.

[79] Hill, R. On discontinuous plastic states, with special reference of localized necking in thin sheets, *J. Mech. Phys. Solids.*, 1952, **1**, 19–30.

[80] Hill, R. Theoretical plasticity of textured aggregates. Mathematical Proceedings of the Cambridge Philosophical Society, 1979, pp. 17.

[81] Han, H.N. and Kim, K.H. A ductile fracture criterion in sheet metal forming process. Journal, *J. Mater. Process. Technol.*, 2003, 142 (1), 231–238.

[82] Narayanasamy, R., Sathiya Narayanan, C., and Parthasarathi, N.L. Some analysis on stress and strain limit for necking and fracture during forming of some HSLA steel sheets *Mater. Sci. Eng. A.*, 2007, 445-446, 427-439.

[83] Clift, S.E., Hartley, P., Sturgess, C.E.N., and Rowe, G.W. Fracture prediction in plastic deformation processes. *Int. J. Mech. Sci.*, 1990, **32**, 1.

[84] Son, H.S. and Kim. Y.S. Prediction of forming limits for anisotropic sheets containing prolate ellipsoidal voids, *Int. J. Mech. Sci.*, 2003, **45**, 1625–1643.

[85] Busk, R.S. Magnesium Production Design, New York, Marcel Dekker Inc., 1986, pp. 13.

[86] Aghion, E., Bronfin, B. and Eliezer, D. The role of the magnesium industry in protecting the environment, *J. Mat. Proc. Tech.*, 2001, **117**, 381–385.

[87] Perez-Prado, M.T. and Ruano, O.A. Texture evolution during annealing of magnesium AZ31 alloy, *Scripta. Mat.*, 2002, **46**, 149–155.

[88] El-Mahallawy, N. A., Taha, M. A., Pokora, E. and Klein, F. On the *influence of process variables on the thermal conditions and properties of high pressure die-cast* magnesium alloys, *J. Mat. Proc. Tech.*, 1998, 73, 125-138.

[89] Hu, B.H., Tong, K.K., Niu, X.P. and Pinwill, I. *Design and optimisation* of runner and gating systems for the die casting of thin-walled magnesium telecommunication parts *through numerical simulation, J. Mat. Proc. Tech.*, 2000, 105, 128-133.

[90] Doege, E. and Droder, K. Sheet metal forming of magnesium wrought alloys formability and process technology, *J. Mat. Proc. Tech.*, 2001, 115, 14-19.

[91] Friedrich, H. and Schumann, S. Research for a "New Age of Magnesium" in the Automotive Industry, *J. Mat. Proc. Tech.*, 2001, 117, 276-281.

[92] Takuda, H., Enami, T., Kubota, K. and Hatta, N. The formability of a thin sheet of Mg–8.5Li–1Zn alloy, *J. Mat. Proc. Tech.*, 2000, **101**, 281–286.

[93] Lee, S., Chen, Y.H. and Wang, J.Y. Isothermal sheet formability of magnesium alloy AZ31 and AZ61, *J. Mat. Proc. Tech.*, 2002, **124**, 19–24.

[94] Kohzu, M., Yoshida, F. and Somekawa, H. Fracture mechanism and forming limit in deep-drawing of magnesium alloy AZ31, *Mater. Trans.* 2001, **42**, 1273–1276.

[95] Won, S.W., Oh, S.G., Osakada, K., Park, J.G. and Kim, Y.S. *2004 Proc. Spri. Conf. Korean Soc. Tech. Plas.*, 2004, pp. 53-56.

[96] Choo, D.K., Oh, S.W., Lee, J.H. and Kang, C.G. *Trans. Mat. Proc.*, 2005, 14, 628-634.

[97] Park, J.G., Kim, J,H., Park, N.K. and Kim, Y.S. Study of forming limit for rotational incremental forming of magnesium alloy sheet, *Metall. Mater. Trans. A., 2009, in-press*

[98] Johnson, G.J. and Cook, W.H. A constitutive model and data for metals subjected to large strains, high strain rates and high temperatures. In: Proceedings of the Seventh International Symposium on Ballistics, The Hague, 1983, pp. 541–547.

[99] Hibbins, S.G. in *Light Metals 1998 Metaux Legers*, Sahoo, M. and Fradet, C.C. eds., TMS-CIM, Calgary, AB, Canada, 1998, 265–8

AIJR Books

About the Author

Associate Professor Nguyen Duc-Toan grew up in Hai Duong, Vietnam. He was educated at the Hanoi University of Technology for his B. Sc. and M. Sc. in the area of Mechanical Engineering. Prof. Duc-Toan completed his Ph. D. at the Kyungpook National University, Korea focusing material behavior and sheet metal forming. Then, he pursued his professional career at leading university of Vietnam (HUST) where he undertook research related to metal cutting, sheet metal forming, electrical discharge machining EDM and CAD/CAM/CAE. Currently, he serves as an Editorial Board Member of a number of societies including JMST Advances (Springer), TNU Journal of Science and Technology and Journal science and technology of Hung yen. Currently, he serves as a Deputy Head of Metal Machining and Industrial instrument. He is also serving as the Vice-president of the Vietnam Association of Science Editing (VASE). Recently, his interest has focused on the material behaviors and its application in industry and Research & Development for mechanical products.

Combined Hardening Behavior for Sheet Metal and its Application

Nguyen Duc Toan

ISBN 978-81-936820-9-8